Effects of Environment on Charge Recombination in Organo-Metal-Halide Perovskite Observed by Photoluminescence Microscopy and Spectroscopy

Li, Jun

2021

Citation for published version (APA):
Li, J. (2021). *Effects of Environment on Charge Recombination in Organo-Metal-Halide Perovskite Observed by Photoluminescence Microscopy and Spectroscopy* (Media-Tryck ed.). [Doctoral Thesis (monograph), Chemical Physics]. Lund University.

Total number of authors:
1

LUND UNIVERSITY

PO Box 117
221 00 Lund
+46 46-222 00 00

Effects of Environment on Charge Recombination in Organo-Metal-Halide Perovskite Observed by Photoluminescence Microscopy and Spectroscopy

JUN LI

DIVISION OF CHEMICAL PHYSICS | FACULTY OF SCIENCE | LUND UNIVERSITY

Printed by Media-Tryck, Lund 2021 NORDIC SWAN ECOLABEL 3041 0903

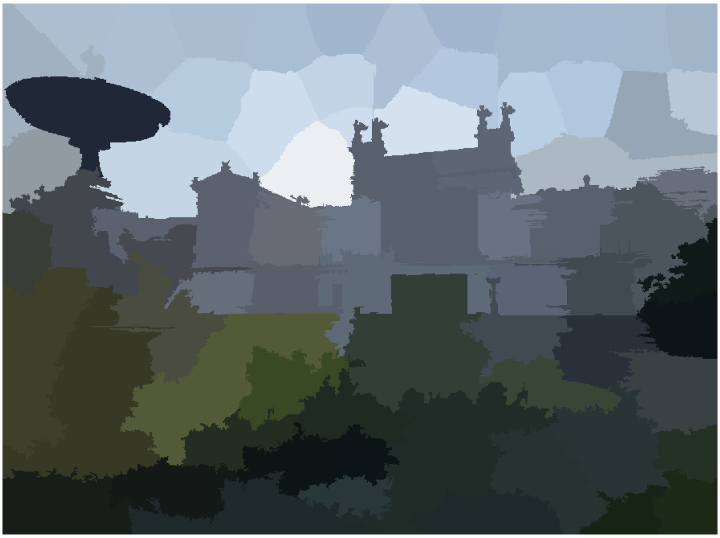

Life is still beautiful! Oh hahaha...

LUND
UNIVERSITY

Faculty of Science
Department of Chemistry
Division of Chemical Physics

ISBN 978-91-7422-788-8

9 789174 227888

Effects of Environment on Charge Recombination in Organo-Metal-Halide Perovskite Observed by Photoluminescence Microscopy and Spectroscopy

Effects of Environment on Charge Recombination in Organo-Metal-Halide Perovskite Observed by Photoluminescence Microscopy and Spectroscopy

Jun Li

DOCTORAL DISSERTATION

by due permission of the Faculty of science, Lund University, Sweden.
To be defended at lecture hall C, Kemicentrum, March 26th, 2021 at 9:15 am.

Faculty opponent
Prof. Hernán Mígues

Organization LUND UNIVERSITY Division of Chemical Physics	**Document name** Doctoral Dissertation
Department of Chemistry P.O. Box 124 SE-22100, Lund, Sweden	**Date of issue** March 26th, 2021
Author Jun Li	Sponsoring organization

Title and subtitle

Effects of environment on charge recombination in organo-metal-halide perovskite observed by photoluminescence microscopy and spectroscopy

Abstract

Organo-metal-halide (OMH) perovskites form a new class of materials with perovskite crystal structure ABX_3 where A is an organic molecule, B is lead (Pb) and X is a halide atom (I or Br). OMH perovskite semiconductors have been widely used in photovoltaics due to their very strong absorption of sun light, very suitable electrical properties, and the ease of preparation. Today the power conversion efficiency of record devices based on OMH is as large as 25.5%.

There are still many challenges for commercial application of OMH perovskite based solar cells and other devices. One of the problems we can formulate as sensitivity of the properties of OMP semiconductors and devices based on them on factors like electric field, atmosphere, light, temperature and so on. Despite large efforts spent in the scientific community on investigation of the environmental effects on OMH perovskites and stability of devices many issues are still not well-understood.

In this thesis, I present results of several research projects where photoluminescence (PL) properties of OMH perovskites were studied by optical luminescence microscopy and spectroscopy under different environmental conditions such as humidity, electric field, local pressure and low temperature. We observed that water molecules can play an important role in the transformation of OMH perovskite from its intermediate phase containing solvent molecules to the perovskite crystal structure. We found that both electric field and local pressure and mechanical damage at nano-scale can create temporal PL quenching in OMH perovskites micro- and nanocrystals. We propose that PL quenching is induced by deep defects states created by electric field, pressure or mechanical manipulation. However, the destructive influence of all these factors on PL disappears several minutes after the influence was stopped due to self-healing properties of OHP. By comparing PL spectra and PL intensity and cryogenic temperatures and at room temperature we found that the concentration of shallow defect states and deep defect states are proportional to each other.

Key words Environment, photoluminescence microscopy and spectroscopy, organo-metal-halide perovskite, charge recombination

Classification system and/or index terms (if any)		
Supplementary bibliographical information		**Language** English
ISSN and key title		**ISBN** 978-91-7422-788-8 (print) 978-91-7422-789-5 (digital)
Recipient's notes	**Number of pages** 166	Price
	Security classification	

Signature Jun Li

Date 2021-02-11

Effects of Environment on Charge Recombination in Organo-Metal-Halide Perovskite Observed by Photoluminescence Microscopy and Spectroscopy

Jun Li

LUND
UNIVERSITY

Coverphoto by Tianyi Wang and Jun Li

Division of Chemical Physics
Department of Chemistry
Faculty of Science

ISBN 978-91-7422-788-8 (print)
ISBN 978-91-7422-789-5(digital)

Printed in Sweden by Media-Tryck, Lund University
Lund 2021

Good food is good mood!

Table of Contents

Abstract

Organo-metal-halide (OMH) perovskites form a new class of materials with perovskite crystal structure ABX_3 where A is an organic molecule, B is lead (Pb) and X is a halide atom (I or Br). OMH perovskite semiconductors have been widely used in photovoltaics due to their very strong absorption of sun light, very suitable electrical properties, and the ease of preparation. Today the power conversion efficiency of record devices based on OMH is as large as 25.5%.

There are still many challenges for commercial application of OMH perovskite based solar cells and other devices. One of the problems we can formulate as sensitivity of the properties of OMP semiconductors and devices based on them on factors like electric field, atmosphere, light, temperature and so on. Despite large efforts spent in the scientific community on investigation of the environmental effects on OMH perovskites and stability of devices many issues are still not well-understood.

In this thesis, I present results of several research projects where photoluminescence (PL) properties of OMH perovskites were studied by optical luminescence microscopy and spectroscopy under different environmental conditions such as humidity, electric field, local pressure and low temperature. We observed that water molecules can play an important role in the transformation of OMH perovskite from its intermediate phase containing solvent molecules to the perovskite crystal structure. We found that both electric field and local pressure and mechanical damage at nano-scale can create temporal PL quenching in OMH perovskites micro- and nanocrystals. We propose that PL quenching is induced by deep defects states created by electric field, pressure or mechanical manipulation. However, the destructive influence of all these factors on PL disappears several minutes after the influence was stopped due to self-healing properties of OHP. By comparing PL spectra and PL intensity and cryogenic temperatures and at room temperature we found that the concentration of shallow defect states and deep defect states are proportional to each other.

Publications included on the thesis

i. J. Li, A. Dobrovolsky, A. Merdasa, E.L. Unger, I.G. Scheblykin, Luminescent Intermediates and Humidity-Dependent Room-Temperature Conversion of the $MAPbI_3$ Perovskite Precursor, ACS Omega. 3 (2018) 14494–14502. doi:10.1021/acsomega.8b01799.

I designed the experiment with IGS, prepared samples and did the whole measurements, data analysis. I wrote the manuscript with IGS.

ii. R. Chen, J. Li, A. Dobrovolsky, S. González-Carrero, M. Gerhard, M.E. Messing, V. Chirvony, J. Pérez-Prieto, I.G. Scheblykin, Creation and Annihilation of Nonradiative Recombination Centers in Polycrystalline Metal Halide Perovskites by Alternating Electric Field and Light, Adv. Opt. Mater. 1901642 (2019) 1901642. doi:10.1002/adom.201901642.

RC designed the experiment with IGS and I did half of the measurements. data analysis and I wrote manuscript together with RC and IGS.

iii. J. Li, M.Galle, P. Frantsuzov, M. Gerhard, T. Basché, I.G. Scheblykin Ultimate self-healing ability of perovskites directly observed via photoluminescence response on mechanical manipulation at nano-scale. (on manuscript)

I prepared samples for this study. M Galle carried out the whole AFM-PL measurement. I did data analysis with the help of M Galle. I wrote the manuscript with M Galle and IGS

iv. A. Dobrovolsky, A. Merdasa, J. Li, K. Hirselandt, E.L. Unger, I.G. Scheblykin, Relating defect luminescence and non-radiative charge recombination in MAPbI3 perovskite films., J. Phys. Chem. Lett. (2020). doi:10.1021/acs.jpclett.9b03878.

I prepared the defect-rich sample for this study and did part of writing for manuscript.

Publications not included on the thesis

i. M. Gerhard, B. Louis, R. Camacho, A. Merdasa, J. Li, A. Kiligaridis, A. Dobrovolsky, J. Hofkens, I.G. Scheblykin, Microscopic insight into non-radiative decay in perovskite semiconductors from temperature-dependent luminescence blinking, Nat. Commun. 10 (2019) 1698. doi:10.1038/s41467-019-09640-w.

I synthesized samples for this study and participate in some results discussion and did part of writing for manuscript.

ii. M. Gerhard, B. Louis, P.A. Frantsuzov, J. Li, A. Kiligaridis, J. Hofkens, I.G. Scheblykin, Heterogeneities and Emissive Defects in MAPbI 3 Perovskite Revealed by Spectrally Resolved Luminescence Blinking, 2001380 (2021) 1–9. doi:10.1002/adom.202001380.

I synthesized samples for this study and did part of writing for manuscript.

iii. I.Y. Eremchev, A.O. Tarasevich, J. Li, A. V Naumov, I.G. Scheblykin, Lack of Photon Antibunching Supports Supertrap Model of Photoluminescence Blinking in Perovskite Sub-Micrometer Crystals, Adv. Opt. Mater. 2001596 (2020). doi:10.1002/adom.202001596.

I synthesized samples for this study and did part of writing for manuscript.

iv. D. Hong, J. Li, S. Wan, I.G. Scheblykin, Y. Tian, Red-shifted Photoluminescence from Crystal Edges Due to Carrier Redistribution and Re-absorption in Lead Triiodide Perovskite, J. Phys. Chem. C. 123 (2019) acs.jpcc.9b03647. doi:10.1021/acs.jpcc.9b03647.

I did some data analysis together with D H and participated some results discussion.

v. A. Kiligaridis, P. Frantsuzov, A. Yangui, S. Seth, J. Li, Q. An, Y. Vaynzof, I.G. Scheblykin, Are Shockley-Read-Hall and ABC models valid for lead halide perovskites?, (2020) manuscript

I synthesized samples for the early stage of this study and did some material characterization (absorption, SEM) for this study, joined results discussion and did part of writing for this manuscript.

Abbreviations

AFM	Atomic force microscope
APD	Avalanche photo diode
CB	Conduction band
CCD	Charge-coupled device
CW	Continuous wave
DMF	Dimethylformamide
EM CCD	Electron multiplying CCD
GBL	gamma-Butyrolactone
$MAPbI_3$	Methylammonium lead iodide
$MAPbBr_3$	Methylammonium lead bromide
NR	Non-radiative
OMH	Organo Metal Halide
PCE	Power conversion efficiency
PL	Photoluminescence
PLQY	Photoluminescence quantum efficiency
PSF	Point spread function
SEM	Scanning electron microscope
SMS	Single molecule spectroscopy
VB	Valence band

Chapter 1 Introduction

1.1 General background

1.1.1 Global energy crisis

Looking back on the history of humans, using fire and making tools are regarded as the turning point of human civilization. History of the human civilization can be also called the history of energy. As one of the most important gifts from nature, fossil energy has already become the main power that supports our daily life during the past thousands of years. In particular, the usage of fossil energy had increased exponentially since the first industrial revolution in the 18th century as shown in Figure 1.1.1. This trend was even rapid in the 1950s when the 3rd industrial revolution was finished.

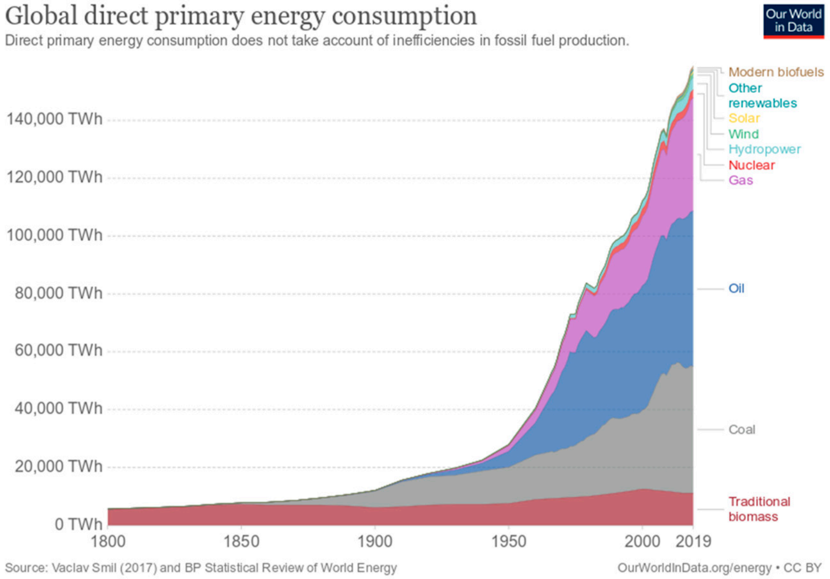

Figure 1.1.1 Global direct primary energy consumption from 1800 until 2019.
(Source: https://ourworldindata.org/energy)

Notwithstanding the human civilization has developed rapidly, emitting products such as CO_2 from fossil fuels has also enlarged simultaneously as shown in Figure 1.1.2. Meanwhile, large number of side effects from excessive use of fossil fuels start to appear. First of all, fossil fuels are non-renewable. Fossil fuels in the earth are formed during the past billions of years. Once they're run out, it is nearly impossible to get them back again. Another problem is the global climate change caused by emission products (CO_2 and other toxic ingredients) from fossil fuels. For example, the greenhouse effects have generated global warming and lead to an increase in the average temperature of the world. Therefore, it is necessary to find some other "clean" energy source that has less carbon emission and is renewable.

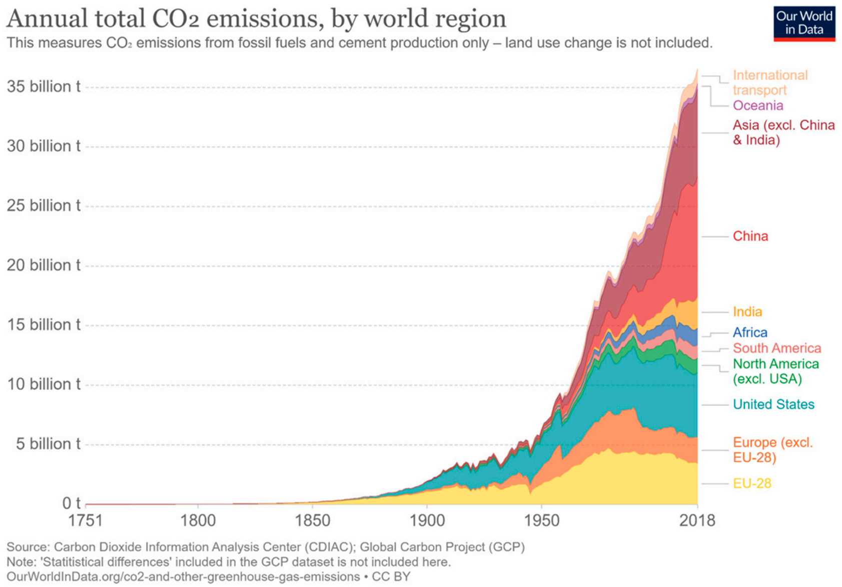

Annual total CO2 emissions, by world region

This measures CO_2 emissions from fossil fuels and cement production only – land use change is not included.

Source: Carbon Dioxide Information Analysis Center (CDIAC); Global Carbon Project (GCP)
Note: 'Statitistical differences' included in the GCP dataset is not included here.
OurWorldInData.org/co2-and-other-greenhouse-gas-emissions • CC BY

Figure 1.1.2 Annual total CO_2 emissions by world region from 1751 until 2018.
(Source: https://ourworldindata.org/energy)

Since the 2nd industrial revolution, the electricity took the place of steam and started to act as the main power source for our daily life. Up to now, almost all of the traditional fossil fuels such as coal were converted to electric power in the power station at first. Besides, new types of fossil fuels such as gas or petroleum were also developed which have higher efficiency and less pollutant emission compared with coal. On the other hand, some other new types of renewable fuels were developed to generate electricity such as nuclear energy, wind, hydropower, and solar energy.

1.1.2 Solar cells and Organo-metal halide perovskites

Among all new energy, solar energy was always regarded as the driving force for all the lives on the earth and has become one of the most important easy-accessed renewable energies in the world. On the one hand, sunlight can drive the photosynthesis reaction in plants to convert the carbon dioxide into oxygen. On the other hand, sunlight can also be converted to electricity via solar cells. Hence, the solar cell is the key to the better use of solar energy as a renewable energy source.

Solar cells were fabricated based on the photovoltaic effect which was first described in 1873 by Willoughby Smith.[1] Almost all of the solar cells use a semiconductor layer to work as a sensor for generating free electrons and holes under the sunlight illumination. Then the generated electrons and holes can be extracted to the anode and cathode of the device to form the output voltage as shown in Figure 1.1.3. Solar cells were applied as power source in many fields since it was fabricated, especially in space crafts or artificial satellite.

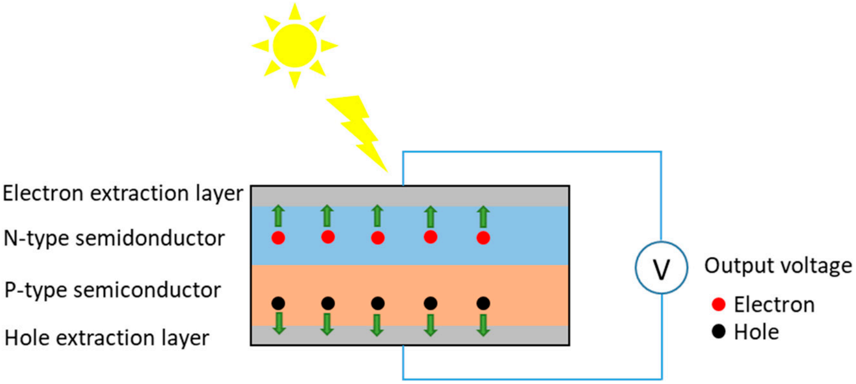

Figure 1.1.3 Scheme figure of semiconductor based solar cells.

The first practical photovoltaic solar cell device was made at Bell Laboratories in 1954. Since then, solar cells started to act as an energy source in space applications (spacecraft or artificial satellite) and in our daily life. During the past half-century, large amount of efforts had been spent to develop different types of solar cells with higher power conversion efficiency (PCE). The PCE of all types of solar cells is presented in Figure 1.1.4. It can be seen that the highest PCE of solar cell reaches 47.1% up to now. However, most of the current solar cells require an extremely low impurity level so that the cost of the solar cell is relatively high. Therefore, developing new types of solar cells with a lower cost has become more and more crucial.

Very recently, organo-metal halide (OMH) perovskite was found to be a potential candidate material for solar cells. Since then, considerable amount of experiments have been done to increase the PCE of OMH perovskite based solar cells and the PCE was increased to 25.5% as marked in Figure 1.1.4.

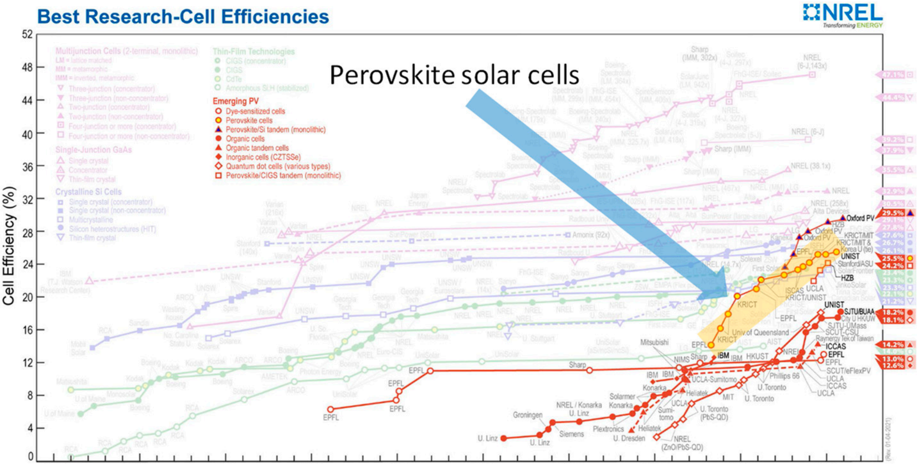

Figure 1.1.4 Figure of best research-cell efficiencies
(Source: https://www.nrel.gov/pv/assets/pdfs/best-research-cell-efficiencies.20200406.pdf)

Despite the great success has been achieved in the OMH perovskite, the fundamental physical properties of this material are still not clear and lead to many mysterious problems. For example, the performance of the OMH perovskite-based solar cell devices might be diverse even if they are synthesized under a similar method, which will be discussed in the latter part[2] The effects of the local environment (such as water in the humid environment) on the OMH perovskite might also be diverse. [3–6] Therefore, systematic knowledge and deeper understanding are required to break the efficiency "bottleneck". Here, some fundamental knowledge about the OMH perovskite will be presented to give a better understanding about this type of materials.

1.2 Introduction to perovskite semiconductors

1.2.1 Introduction to perovskites

Perovskite is one kind of calcium titanium oxide mineral which was originally discovered in 1839 in Russia by Gustav Rose and the name came from Russian mineralogist Lev Perovski. The chemical formula is $CaTiO_3$ and the cubic crystal structure is presented in Figure 1.2.1, in which Ti and O forms $[TiO_6]^{8-}$ octahedral and Ca^{2+} locates in the space between octahedral. This type of crystal structure was named perovskite structure. Now "perovskite" is not only the name of this calcium titanium oxide mineral, but also for all the materials with such type of crystal structure. For example, $BaTiO_3$[7] and $BiFeO_3$[8] are the compounds which have the similar ABX_3 formula and the same crystal structure. Among all kinds of perovskite compounds, OMH perovskites have become prominent because of their excellent performance in the fields of solar cells, LEDs, lasers and so on. [9]

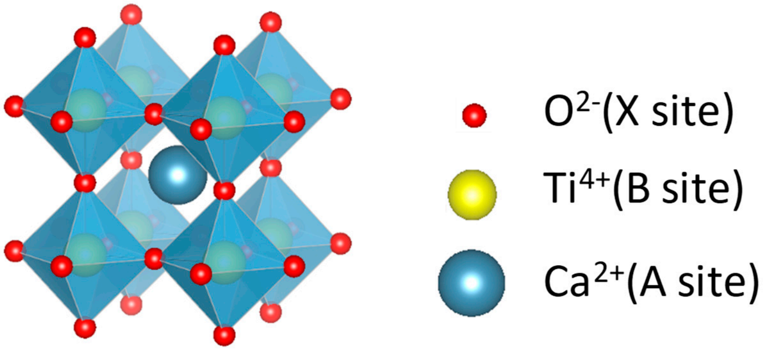

Figure 1.2.1 Crystal structure of $CaTiO_3$ perovskite

1.2.2 Organo metal halide (OMH) perovskites

1.2.2.1 What are Organo metal halide perovskites

Organo metal halide (OMH) perovskites are one kind of novel compounds which owns the perovskite structure. Here, *A* site is occupied with organic cation such as methylammonium. *B* site is metal cation (Pb, for example) and *X* site is halide anion. One typical OMH perovskite is methylammonium lead triiodide ($MAPbI_3$, $MA^+=CH_3NH_3^+$), in which Pb and I form $[PbI_6]^{4-}$ octahedral and further form the inorganic framework. MA^+ occupies the space in between. I^- can also be replaced by other halide anions such as Br^- or Cl^- and MA^+ can be replaced by other cation like Cs^+. The structural stability can be described by $t = (r_A + r_X)/\left[\sqrt{2}(r_B + r_X)\right]$

and the Goldschmidt tolerance factor (t) is based on the relationship between the radius of each site and r_A, r_B and r_X are the radius of A, B and X, respectively[10,11]. The $MAPbI_3$ shows the cubic phase (as shown in Figure 1.2.2) under 329 K. At room temperature, the $[PbI_6]^{4-}$ octahedral may show a slight distortion, leading to the formation of tetragonal structure. If the temperature goes even lower to about 160 K and 170K, the distortion will be even more to form an orthorhombic structure. The comparison of two different $MAPbI_3$ phase is presented in Figure 1.2.2.

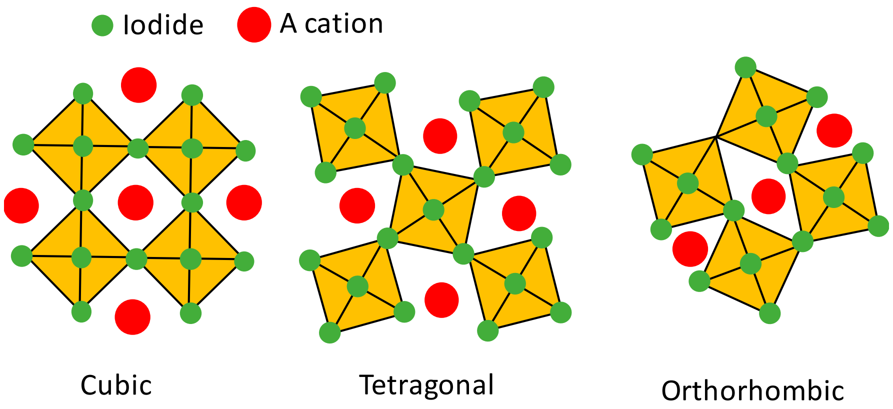

Figure 1.2.2 Scheme figure of the cubic, tetragonal and orthorhombic structure of $MAPbI_3$ perovskite.

1.2.2.2 Semiconductor properties of OMH perovskites

Before discussing about the electronic structure of the perovskite, let’s take a look of the energy level splitting of two atoms at first. Assume that we have two identical atoms with one energy level. When they are far away from each other, their energy levels are identical. However, when they are put closer, the energy levels will overlap and split into two levels because of the Pauli Exclusion Principle, which says that there mustn’t be two electrons which have exactly the same energy levels at the same time. Followed by this idea, if several atoms (N) are brought together, the energy levels of each atom will also overlap and split due to the interaction between atoms, resulting in N types of separation but closely spaced energy levels. If N is extremely large, these energy levels will become a continuous energy band, as shown in Figure 1.2.3 (a).

When it comes to semiconductors, things will be much more complicated as more orbits from each atom may contribute to orbital overlap to form energy bands. The electrons occupy the lower energy bands and the higher energy bands is not occupied (Or occupied by holes). The highest occupied band is called valance band (VB) and the lowest unoccupied band is named conduction band (CB). The gap between the valence band maximum (VBM) and conduction band minimum (CBM) is called bandgap, as illustrated in Figure 1.2.3 (b).

As mentioned in the previous text that the VB and the CB are occupied by electrons and holes, respectively. Since almost all the electron states in VB are fully occupied, the electrons cannot move freely in VB. But if the electrons are excited into the CB, they can move freely because there are lots of unoccupied electron states. In $MAPbI_3$, the Pb-6*s* and I-5*p* orbits forms the VB while the CBM is formed by the Pb-6*p* and I-5*p* orbits with the bandgap of about 1.6 eV [12]. So it is the Pb-I inorganic frame work that mainly contributes to the electronic properties while the effect of MA^+ is negligible, [12] but the orientation of MA^+ can affect some physical properties such as dielectric constant.[12] There are quite many factors which can affect the electronic structure such as substitution or mixture of different halide anion,[13,14] the unpaired bond (or also called defect) [15,16] and the external pressure.[17–19]

If there is no momentum shift between CBM and VBM, this can be called the direct semiconductor, such as GaAs [20], otherwise it is the indirect semiconductor, such as Si [21]. The OMH perovskite such as $MAPbI_3$ was considered as direct semiconductor. [17,22–24]

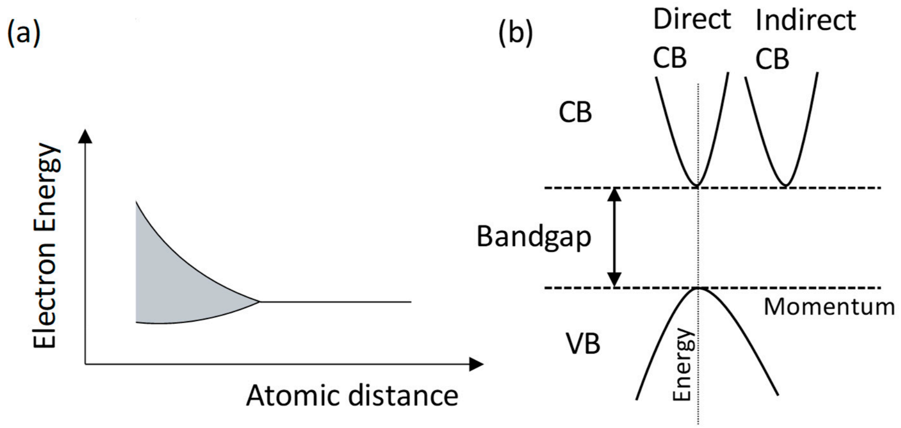

Figure 1.2.3 (a) Scheme figure of splitting of energy level into a band**. (b)** Scheme figure of direct and indirect bandgap semiconductors.

1.2.2.3 Absorption and photoluminescence in OMH perovskites

Due to the unique band structure, the OMH perovskite has a wide absorption spectrum which covers almost all visible light wavelength region and a high absorption coefficient (10^5 cm^{-1}) as shown in Figure 1.2.4 (b) with black solid line[25], where an absorption edge was clearly presented here. When the OMH perovskite is being illuminated by the light which photon energy is greater than the bandgap energy, some of the electrons in the VB can be excited to the CB with holes left in the VB. As mentioned in the previous text that electrons and holes can move freely in the CB and VB respectively with several hundreds of nanometer diffusion length.[26] This is key point to the application of solar cell devices. The excited electrons can relax to the bottom of the CB in a very short period (about fs to ps) as marked in Figure 1.2.4 (a). Then they can recombine with hole via either a radiative recombination process with photon emission or a non-radiative (NR) recombination process in the trap state, which leads to the NR energy loss. The PL spectra of the $MAPbI_3$ perovskite is shown in the red dash line in Figure 1.2.4 (b) and the photon energy of the PL emission peak is around 1.6 eV. PL is a very important tool for us to understand more about charge recombination process happened within the material.

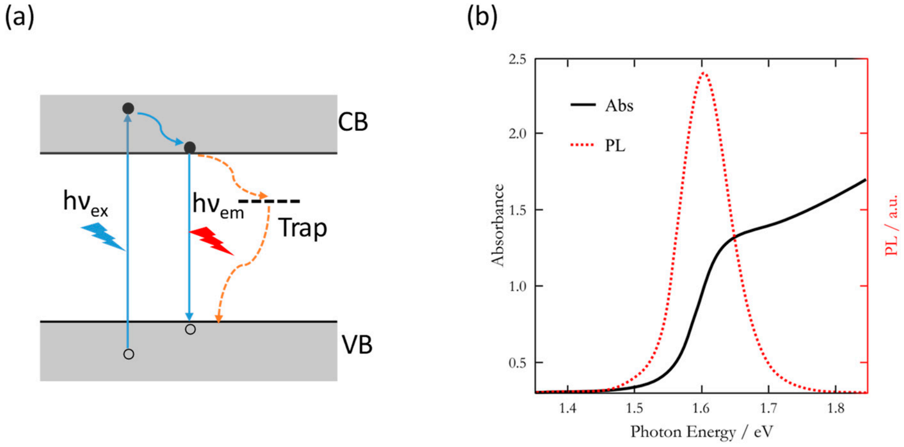

Figure 1.2.4 (a) Charge trapping and recombination process in semiconductors**. (b)** PL and absorption spectra of $MAPbI_3$ perovskite [27]

1.2.2.4 Migration of defects and ions in OMH perovskites

As one of the most import intrinsic properties of OMH perovskite, defects have already become a "hotspot" and have attracted considerable amount of the attention in both the theoretical and experimental fields because of their direct influence in the performance of the OMH based solar cell devices. [15,16,28–31] Defect tolerance is one of the unique properties in OMH perovskite which contribute to their great performance in solar cells.[31–33] In order to understand the mechanism behind this, knowing the intrinsic properties of defects is required.

From the view of crystallography, defects describe the interruptions of the periodic structure pattern in crystalline solids. Crystallographic defects include point defects, line defects, planar defects as well as bulk defects based on their dimension. In the OMH perovskite, the point defects are rather important as they act as quenchers during the non-radiative quenching process. There are quite many types of point defects in OMH perovskite, including the vacancies, interstitials of halide anion, organic cation and metal cation. Antisite defects are also one of the typical point defects in OMH perovskite that the position of one ion was replaced by another one. The scheme of these point defects is shown in Figure 1.2.5 (a). Among all of point defects, halide vacancies (V_I) and halide interstitials (I_i) seem to have lower formation energy according to the previous theoretical calculations[34,35] and experimental results[36], which means that they are easier to be formed in the OMH perovskite crystal. Figure 1.2.5 (b) shows the thermodynamic ionization levels of different point defects in $MAPbI_3$ perovskite crystals. It can be indicated that V_I, Pb_i and MA_i locate close to the CBM ("shallow trap") while I_i and V_{Pb} are in the middle of the bandgap ("deep trap"). Generally speaking, "deep trap" can act as NR recombination centre because both electrons and holes can be captured here. In contrast, "shallow trap" locates quite close to the edge of CB or VB which allows them easier to capture the electrons. However, the probability to capture a hole from VB to this state is quite low as shown in Figure 1.2.5(c). In this case, these traps do not act as NR recombination centre and the electrons might "escape" from "shallow trap" back to the CB. This is quite unique in perovskite compared with other traditional semiconductors.

Now here comes a question, why there are so many point defects in the OMH perovskite crystals? In fact, these defects might be formed during the crystallization from solution process. [2] In Section 3.4, we will compare the PL of OMH perovskite film under low temperature, where the relationship between defects and synthesis method will be discussed. Another mechanism for the formation of the point defects is the ion migration, which has also been widely studied in the previous reports. [37–40]

Based on the fact that photoluminescence quantum yield (PLQY) of most OMH perovskite films are quite low (about 1 % or less), it can be indicated that most of the input energy from incident light are lost due to NR recombination process. On the other word, these traps are quite efficient to “kill” most of the PL. Here comes another question, why is NR recombination process so efficient in OMH perovskite? In OMH perovskite, charge carrier diffusion length is longer than the distance between NR recombination centres. Besides, the capture and recombination cross-section of the non-radiative recombination centre is strong.[41]

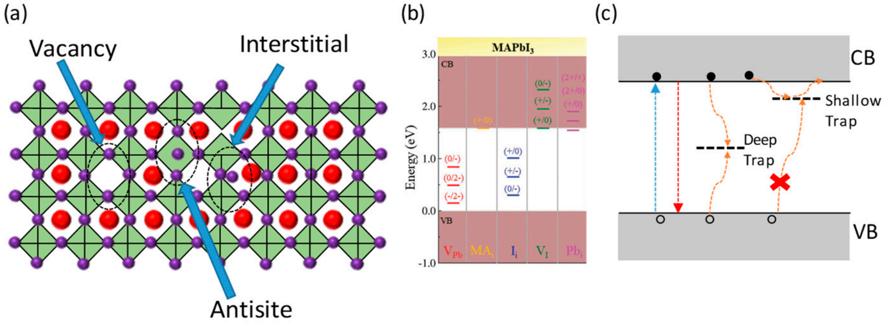

Figure 1.2.5 **(a)** The scheme figure of different point defects in OMH perovskite**.** **(b)** Thermodynamic ionization levels of most stable defects in MAPbI$_3$.[31] **(c)** The scheme figure of trap-assisted recombination process.

1.2.3 Synthesis methods of OMH perovskites

1.2.3.1 Different synthesis methods for OMH perovskites

Different from other semiconductors, OMH perovskite films can be synthesized via solution method so that the cost can be significantly reduced. The most widely used method is one-step method as shown in Figure 1.2.6.[42–46] In this method, the raw materials (Pb-halide compounds, MA/FA-halide compounds) were dissolved in some organic solvents such as dimethylformamide (DMF) or gamma-Butyrolactone (GBL) to form precursor solution at first. Then the precursor solution was spin-coated on the pre-cleaned substrate. After thermal annealing to remove the solvents, the perovskite samples were prepared. Furthermore, this preparation method was improved by changing components such mixing different types of A-site ions as well as halide ions. [47–50] Anti-solvent annealing process was also introduced to further improve the photovoltaic performance of OMH perovskite films [51–53].

Another widely-used solution method to prepare OMH perovskite films is the two-step methods, [54–58] in which Pb-halide compounds and MA-halide compounds were dissolved in two different solvents separately at first. Then Pb-halide precursor was spin-coated on the substrate to form film. In the end, MA-halide solution was dropped on the Pb-halide film to form perovskite films. In some recipe, this procedure can also be achieved by dipping the Pb-halide film into the MA-halide solution to form perovskite film.

There are also many other methods such as chemical vapor deposition method to prepare perovskite films. [43,59]

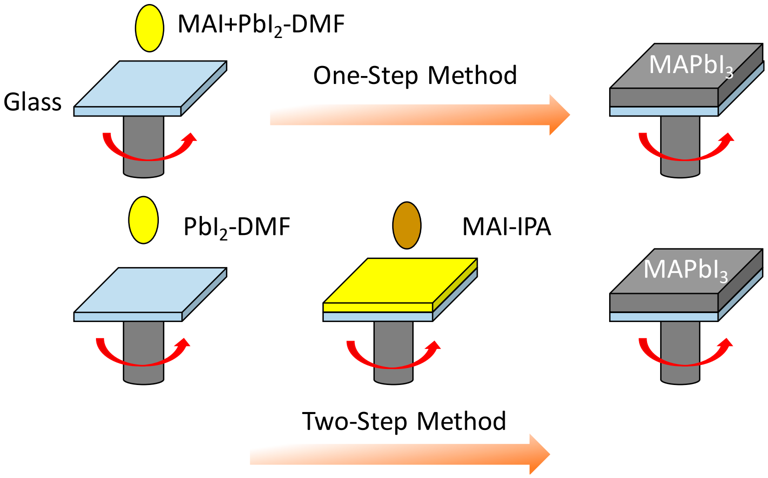

Figure 1.2.6 Scheme figure of one-step and two-step method for synthesis of $MAPbI_3$ perovskite films.

For most of the solar cells, the concentrated $MAPbI_3$ films with high surface coverage rate are always required, even lots of improvements in synthesis such as anti-solvent treatment was used to get better coverage or larger grain size.[51,60–63] For some of the studies which is based on the results from a large area (such as the PL distribution in a large area), this sample is perfect. However, if we want to study size-dependent properties of perovskite such as the effect of trap to the charge carrier recombination process under optical microscopy, these large samples are not proper anymore. As is mentioned in the previous text that chargers have a quite long diffusion length in perovskite, the effects of traps to chargers recombination process will be more pronounced if charges are limited in a small region nearby traps. Furthermore, if the film is not homogeneous, the diversity of intrinsic properties from different micro region could be ignored due to the “average” information. Therefore, it is necessary to make a low concentration film instead to obtain individual perovskite “islands” to beyond the ensemble average. In addition, the unique spatial resolution from PL microscopy and spectroscopy (which will be discussed in later chapter) could tell more information about the intrinsic properties (such as charger carrier dynamics) of OMH perovskite from these individual “islands”. In this study, both the high and low concentrated $MAPbI_3$ films samples were synthesized. More detailed recipe about synthesis will be found in Section 2.3

1.2.3.2 Effects of solvents to crystallization of OMH perovskites

When preparing high concentrated $MAPbI_3$ films with one-step method, there are several candidate solvents (such as DMF, DMSO or GBL) for this process.

However, it has been already known that different solvent may result in different film morphologies.[64–67] The general picture is like this: When PbI_2 and MAI are dissolved in the solvent, the solvent molecule will form the coordination bond with Pb to form the solvent-$MAPbI_3$ intermediate phase. The further crystallization is based on the intermediate phase. Therefore, the morphology and even performance of the final perovskite are determined by the intermediate phase structure. Figure 1.2.7 illustrates the solvent-based intermediate phase during the transition between PbI_2 and $MAPbI_3$ using DMSO and DMF. It can be indicated that the formation of perovskite film from solution is quite complicated.

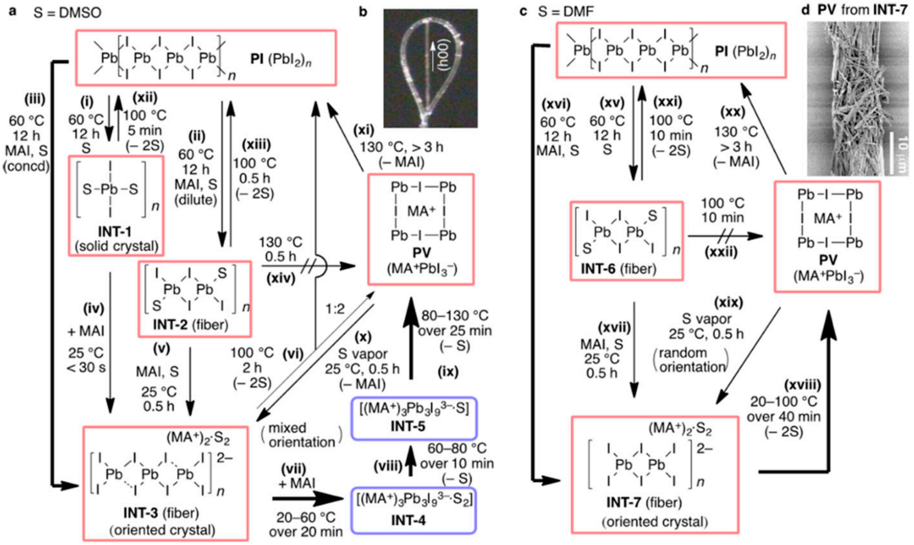

Figure 1.2.7 Chemical reactions between PbI_2 and $MAPbI_3$ mediated by DMSO and DMF studied for isolated crystalline intermediates.[64]

1.3 The importance of this study

Despite numerous efforts, such as changing chemical component [50,68–70] or changing solution process with chemical vapour deposition [62,63,71,72], have been spent to improve the performance of the OMH based solar cells, their still exists lots of shortcomings which limit the application of OMH based perovskite solar cells. One of the serious issues comes from their poor long-term device stability, which is mainly affected by the surrounding environment.

For example, water and humidity of the atmosphere are essential to the OMH perovskites. On the one hand, water is a great challenge to the stability of OMH perovskite solar cell devices as it can induce the degradation of the perovskite. On the other hand, water can also act as one of the anti-solvents during the crystallization process and lead to larger grain size. [73–76] In addition, thermal annealing is always required during synthesis of the OMH perovskite while water can provide a possibility to remove thermal annealing to reduce energy cost.[42,77] By tracking the PL spectra and image of OMH perovskite during crystallization process under different humidity, we can track the transition of perovskite from the intermediate phase. More detailed discussion can be found in Section 3.1.

Electric field (EF) is another important environmental factor to the stability of the OMH perovskite which can induce ion migration inside.[37,78–80] The EF induced ion migration might change the internal electric field within perovskite and lead to the change in the light current-voltage characteristics. Furthermore, EF can induce reversible conversion in OMH perovskite phase[78]. In this case, when the external EF was removed, all the "side effects" will disappear and perovskite will recover to the initial state via ion migration. However, in most of previous studies, perovskite film was in direct contact with electrodes which made it difficult to tell the effect of pure electric field to the charge injection induced decomposition because of the lack of the insulation layer. In order to solve this problem, an insulation layer between electrodes and perovskite should be introduced. This part will be discussed in Section 3.2.

Another effect which is related to the stability of the perovskite is the local pressure and has been discussed in lots of previous studies.[81–87] It is known that external pressure can induce the phase transition in OMH and change the electronic band structure by changing the crystal lattice constant. [18,19,88–90] What's more, the internal pressure (crystal strain) might be formed during the crystallization process and it can enhance NR recombination rate by providing a driving force for defect formation. [81–87,91] In order to study the effect of pressure to the PL of perovskite, a confocal microscope system embedded with an AFM is used in this study (or also shown in Section 2.2.3). Here, the AFM tip was used for both pressing crystal as well as scanning crystal surface morphology. More detailed discussion can be found in Section 3.3.

Temperature is also one of the unavoidable environmental condition which may affect the properties of OMH perovskite. [92–95] If OMH-based solar cell device was used in the space out of the earth, the temperature change would be quite significant. There are quite lots of effects related to the environmental temperature on the OMH perovskite. For example, phase transition has been reported in previous studies which may appear in OMH perovskite under a certain temperature (also called phase transition temperature). [2,93,96] Moreover, there exist lots of traps on the perovskite. When the OMH perovskite is placed at low temperature, the emission from these trap states can be detected to help us to understand more about the properties of defects in OMH perovskite. More detailed discussion can be found in Section 3.4.

As being mentioned in the previous text that the PL is as an important indicator for the charge carrier recombination kinetics of OMH perovskite, which is closely related to the device efficiency. Meanwhile, PL microscopy and spectroscopy was used as the main characterization instrument due to its advantage in PL study which will be discussed in next chapter. We believe that studying the PL of OMH perovskite under different environmental conditions with PL microscopy and spectroscopy can provide more fundamental knowledge about how the environment affects the performance of OMH perovskite. For further characterization, scanning electron microscope (SEM), atomic force microscope (AFM) and other techniques will be applied.

Chapter 2 Experimental Setup

2.1 Optical and PL microscopy

Microscope is one kind of instruments from which one can see very small objects with naked eyes. Optical microscope is the traditional microscope which uses visible light as the light source and the image magnification is achieved by an optical lens. Electron microscope was developed in the 20th century which uses the electron beam to scan the surface of the small objects and get high magnification images, such as scanning electron microscopy (SEM) and transmission electron microscopy (TEM).

The simplest optical microscope system is just an optical lens, which has been widely used in our daily life such as reading a newspaper with a magnifier for example. However, the magnification is limited and can only reach to about 30X. Later, the compound microscope was developed which contains one eyepiece lens and one objective lens and the total magnification can reach to several hundred times. In this section, the PL microscopy will be mainly discussed as it is the fundamental characterization instrument in the whole study.

2.1.1 Principle of PL microscopy

Compared with other optical microscope which collects reflection light from the sample surface, PL microscope collects the PL signal instead. If a sample (also called fluorophores) was illuminated by a light with a specific wavelength (e.g., monochromic laser), it would absorb and emit the light with a longer wavelength, which is called Stocks shift [[97]]. Therefore, one can separate the excitation light and emission light by using proper optical filters such as a dichroic mirror.

Figure 2.1.1 (a) shows the picture of an upright PL microscope (Olympus BX61) and the scheme figure is shown in Figure 2.1.1 (b). The incident light was first selected by the excitation filter. Then the selected light with the certain wavelength (purple line) was reflected by a dichroic mirror and focused on the sample by the objective lens. The emission light (yellow line) from sample was collected by the same objective and propagated through the dichroic mirror. Then the emission light was cleaned by an emission filter and focused on the detector by the image lens. From this setup, one can take the luminescence image of the sample.

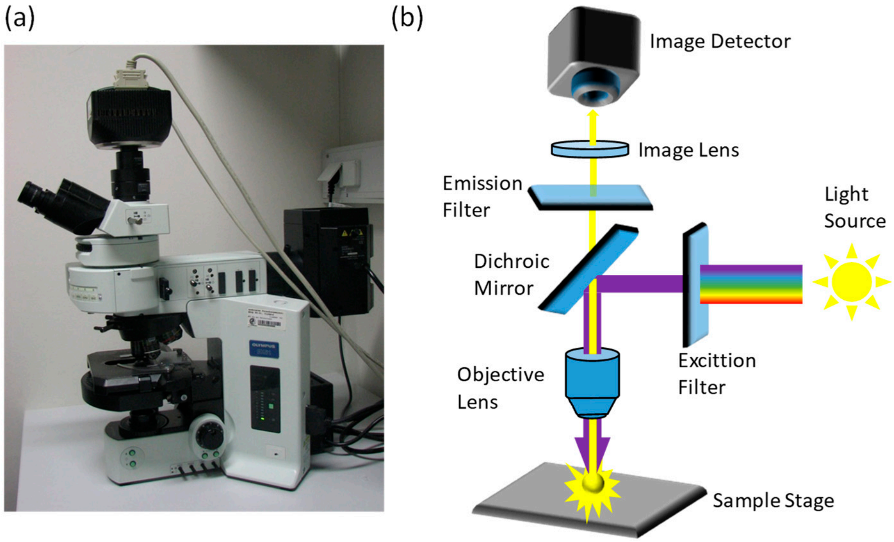

Figure 2.1.1 (a) Picture of PL microscope. (image source: https://en.wikipedia.org/wiki/Fluorescence_microscope). **(b)** Scheme figure of luminescence microscope

2.1.2 PL microscopy and spectroscopy

The PL microscopy and spectroscopy used in the whole study was built based on an Olympus IX71 optical fluorescence microscope, as shown in Figure 2.1.2 (a) and the scheme figure of the setup was presented in Figure 2.1.2 (b). Compared with the normal PL microscope as shown in Figure 2.1.1, our PL microscopy and spectroscopy can get not only PL image, but also the absorption or emission spectroscopy as well as PL decay curves.

In this setup, both continuous-wave (CW) and pulsed laser were used as the light source. For CW laser, 514 nm CW excitation line from the Argon laser was used in the whole study. The excitation spot size was approximately 40 μm in diameter at the sample plane and the power density was varied from 0.2 to 3.6 W/cm^2. For pulsed excitation, 485 nm from diode laser was used in the whole study and the repetition rate was varied from 2.5 to 80 MHz. Other laser sources with different wavelength (640 nm, 405 nm, …) or repetition rate are also available in this setup.

The function of all optical components in this setup are presented as follow. Here, the laser was introduced and focused on the sample stage of optical microscope by a dry objective lens (40X, Olympus LUCPlanFL, NA=0.6). A neutral density filter wheel was placed in the excitation beam path to control the excitation power. Next, a defocusing lens was then placed behind the neutral density filter to magnify the excitation spot to obtain a wide-field image. If without defocusing lens, the full laser power will be focused on a small point and lead to a high-power region which may damage the sample. Then an excitation clean-up filter was placed between the microscope and the defocusing lens to purify the excitation laser light. In order to separate the excitation light and emission light, a dichroic mirror was installed inside the microscope to block the excitation laser and transmit the emission light as shown in the setup figure. Then the emission light transmitted from dichroic mirror was guided to the detection light path by a reflection mirror. and cleaned by an emission clean-up filter in the detection path.

In this setup, an EM-CCD (electron multiplying CCD, ProEM 512B, Princeton Instruments) was used to collect photons or images which was magnified by the image lens as marked by L2 which could give 2X magnification. For the CCD camera, the size of each pixel in the detection chip was 16 μm by 16 μm and the effective pixel size of the CCD chip under 40X objective lens was calculated to be 200 nm. ($16 \div (40 \times 2) = 200nm$). With this effective pixel size, we can estimate the size of the area and determine the excitation power density.

In this setup, one can record the PL intensity change with time by recording movie via EM-CCD. Then we can get the PL transients of the whole region or a small region. We can also add a long-pass, short-pass or band-pass filter in the emission detection path to get the distribution of components with certain emission wavelength. (See Section 3.4 for example)

To measure the PL spectra, a slit was placed in the detection path. The width of the slit was adjusted as narrow as possible to get a narrow vertical light. Then the narrow vertical light transmits through a diffraction grating (150 grooves/mm) which was placed in front of the CCD camera. Due to the light diffraction effect, the interference of light transmitted from each groove would lead to the spatially separated fringes in the CCD detection screen (also called first-order fringes) with a bright zero-order fringe which does not show any position shift. The obtained image from CCD was the PL spectral image, see Figure 2.1.2 (c) for example. The PL spectra could be converted by counting the distance between the zero-order and first-order diffraction fringe in horizontal direction. Here, the distance was counted by pixel. In order to convert it to wavelength unit, the spectral resolution needed to be obtained at first. We used this setup to measure the PL spectra of the light from mercury lamp in the lab. By taking the wavelength of the known spectra line divided by the horizontal distance between zero-order and first-order spectra line, we can get the calibrated spectral resolution. In our setup, the resolution was about 2.09 nm/pixel. By selecting different regions in vertical direction on the PL spectra image, we can get the spatial-resolved PL spectra of the sample.

For PL decay measurement, a 50/50 beam-splitter was placed between the image lens and the CCD camera to split half of the emission signal to the APD (Avalanche Photodiodes, Single Photon Avalanche Diode, PicoQuant) detector. Then a pinhole (100 μm diameter) was placed to block majority and only allow the emission light from a small region of the sample to pass. The image lens L3 was installed to focus the light passed through a pinhole into the APD detector. By checking the corresponding coordinates of the pinhole in the CCD screen, one can put the interested region of sample in the coordinates by moving the sample stage or imagine lens and measure the PL decay from this position. The effective diameter of the pin hole was 1.2 μm if under 40X objective lens. This pinhole could also be removed if we want to get average signal from a large area. In this setup, the pulsed laser and APD detector were connected and controlled by a Time Correlated Single Photon Counting (TCSPC) system from PicoQuant PicoHarp 300 counting module and the time resolution is about 100 ps.

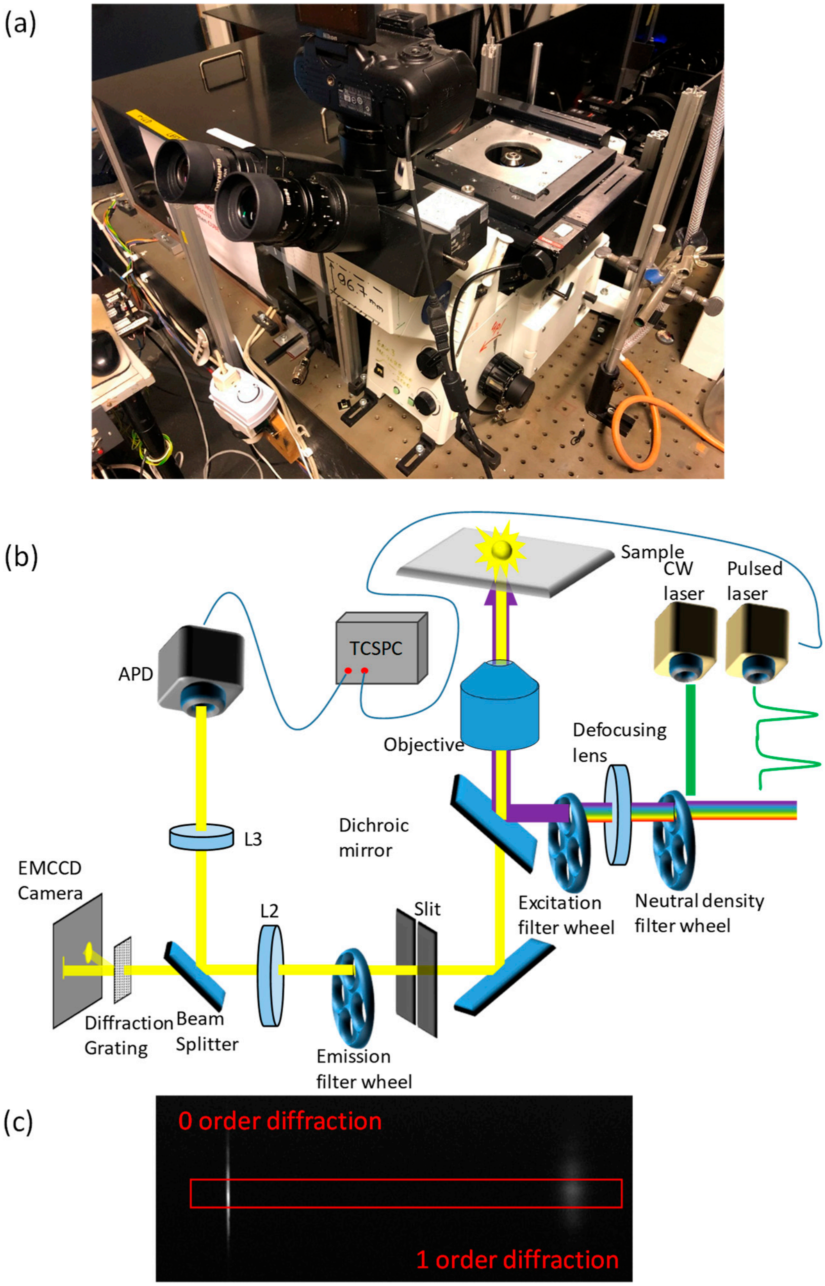

Figure 2.1.2 Image **(a)** and scheme figure **(b)** of photoluminescence microscopy and spectroscopy used on this study. **(c)** An example of PL spectra image obtained from CCD camera.

2.1.3 Advantage of PL microscopy and spectroscopy for material science

In other PL measurements such as the PL spectrometer, the sample was often placed in the sample stage and the signal was obtained from a large area. This is okay for homogeneous sample. However, if the sample is not homogeneous, some extra information will be "hidden". In this case, the advantages of the fluorescence microscopy start to appear. First of all, we can get reflection image and PL image of a sample so that we can check the surface morphology as well as the PL intensity distribution. By adding proper optical filters, we can get spectrally filtered PL image to see the distribution of different phase or component with different PL emission peak. (See the description in Section 3.4 and Paper IV). One can also get PL spectra by adding a diffraction grating in the front of the CCD camera. By changing the position of the slit, we can get the PL spectra from different region of the samples. Similarly, we can get PL decay curves from different region of the samples by changing the pinhole position in the detection path. By adding cryostat with transparent windows, we can get PL data under different temperature (See description in Section 3.4 and Paper IV).

One typical example to show the PL microscopy and spectroscopy in material science is the research of PL blinking of OMH perovskite nanocrystals in our previous studies.[95,98] In these studies, the CCD camera was used to collect PL transients of $MAPbI_3$ nanocrystals by recording a movie while each frame of this movie corresponds to one PL image of the crystal. After further mathematical analysis based on these images, the PL blinking model was developed.[98] By changing the temperature, the temperature dependent PL transients can be also collected from the same setup and the corresponding switching mechanism was formed.[95] The PL spectra of the OMH perovskite was also obtained from this setup even under temperature and this was used to study the PL of $MAPbI_3$ nanowires under different temperature, in which the relationship between the temperature and activation/passivation of traps was studied.[99]

2.2 Other setups used in this study

2.2.1 Home-built humidity controller

The humidity of the local environment surrounding the OMH film was controlled by a home-made humidity controller as shown in Figure 2.2.1. The main dry N_2 tube was divided into two branches. On one branch, the N_2 was introduced into water. After bubbling in the water, the N_2 in this branch will become humid. Another branch was still the dry N_2. In the end, these two branches of N_2 mixed with each other by valves. By controlling the valve, the ratio between dry and humid N_2 could be changed and lead to the change of the humidity in the end. The humidity value was measured by a commercial hygrometer and the accuracy was about 10%. The N_2 with designed humidity was then pumped into a closed sample chamber.

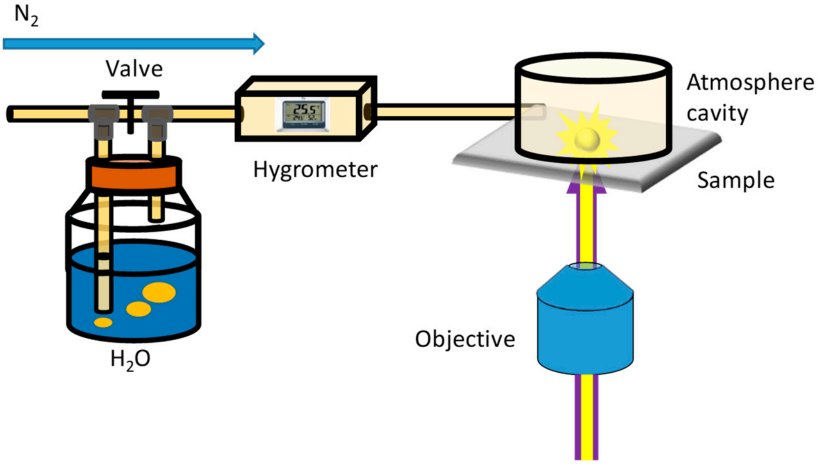

Figure 2.2.1 Scratch figure of home-made humidity controller used on this study.

2.2.2 Devices with interdigitated electrodes

The device with interdigitated electrodes used in this study was fabricated on the SiO_2/Si wafer by standard photolithography method. The device was mounted on the optical microscope as shown in Figure 2.2.2 (a). The positive photoresist was spin-casted on the bare substrate and baked at first. After photolithography process, a pattern of interdigitated electrode was printed on the photoresist-covered substrate. Next, a Ti (5nm)/Au(200nm)/Ti(5nm) metal layer was deposited on the substrate by thermal evaporation process. Then the substrate was soaked in acetone to remove residual the photoresist and metal layer to obtain the interdigitated finger-pattern metal electrodes. In the end, 140 nm SiO_2 layer was applied to cover the surface via plasma enhanced chemical vapour deposition process to act as an insulation layer. The width of the metal bar was 5 μm and the height was 210 nm. The space between metal bar is 5 μm.

In order to generate electric field (EF) between the electrodes, a functional generator was used to generate either constant or alternating EF in this study. Then the voltage signal was amplified 10 times by an amplifier connected to the function generator. An oscilloscope was also connected to the amplifier to monitor the frequency and the amplitude of the signal. The scheme figure of constant and alternating EF was shown in Figure 2.2.2 (b). The actual EF distribution between electrodes under 50V constant was simulated and shown in Figure 2.2.2 (c). It can be indicated that strong EF is generated on the edge of electrodes only.

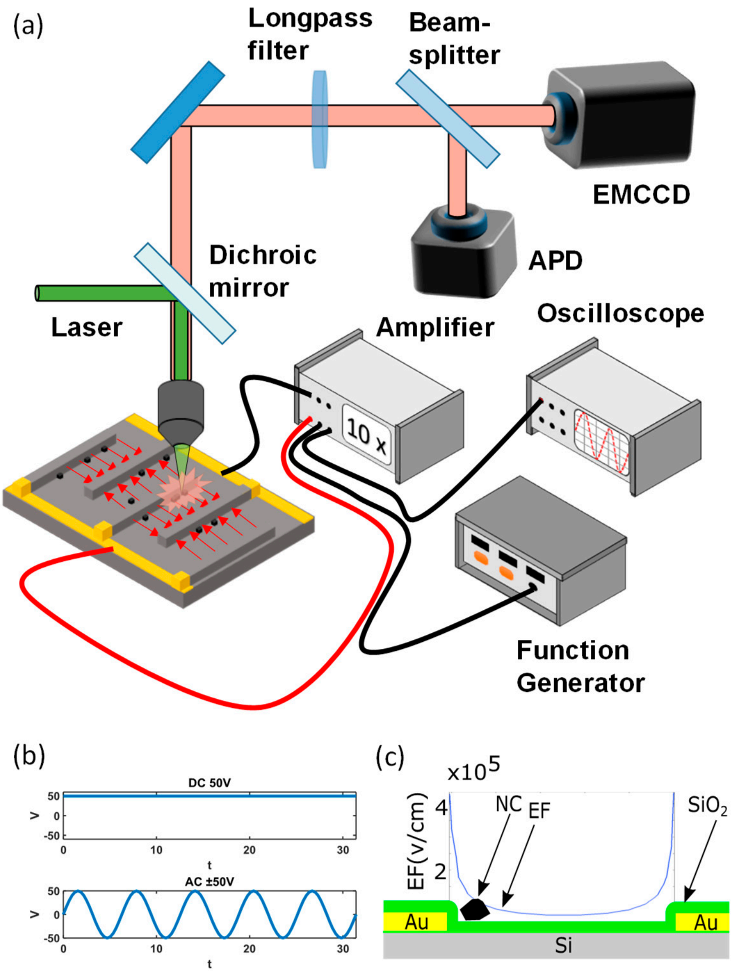

Figure 2.2.2 (a) Scheme figure of the interdigitated electrode device with microscope. **(b)** Two types of bias voltages applied to the interdigitated electrodes device. **(c)** The scheme of the device (not in scale), thicknesses of the layers: Au—210 nm, SiO_2—140 nm. The distribution of the EF over the electrode gap is calculated for 50 V constant voltage applied between neighboring electrodes using COMSOL simulation software. Close to the electrode edge, the EF reaches 4×10^5 V cm^{-1}

2.2.3 AFM-PL microscopy

In this subproject, the atomic force microscope (AMF) and confocal PL microscope were combined together to study the OMH perovskite nanocrystals as presented in Figure 2.2.3. This setup is available in Mainz University and we got the permission to use it for our study.

The experimental setup (Figure 2.2.3 a) consists of a home-built confocal microscope and a commercial AFM (MFP-3D, Asylum Research) mounted on the top of the sample stage of an inverted confocal microscope. Silicon tip with radius of 7 nm (OPUS 240-AC-NA-100, MikroMash) was used for probing the topology and for pressing and cutting the sample. The sample was excited by a CW diode laser (640 nm) giving 0.45 W/cm^2 excitation power density at the sample stage after being focused by an oil immersion objective lens (1.4 NA, 100X, Zeiss). The objective lens can be moved by a three-axis piezoelectric translation stage. The sample holder is placed on top of a two-axis piezoelectric translation stage (belonging to the AFM). Light emitted by the sample is collected by the same objective and sent through a short-pass (to block the NIR laser used in the AFM) and a long-pass filters to remove the excitation light. Then the emission was guided to a photon counting detector (APD, SPCM-AQRH-15, Perkin Elmer) and a spectrograph with a CCD camera. Except of the lasers and the spectrograph with the CCD, the whole setup is placed on a vibration isolation table and its temperature stabilized at 28 °C by a closed isolated box.

It is important to realize that AFM tip is probing/manipulating the top surface of the sample, while PL is excited and collected from the other side, through the glass cover slip (Figure 2.2.3 b).

The setup was used in three different modes where the excitation laser spot was focused to the X-Y position of the AFM tip:

Imaging mode: In this mode, the AFM was used in the tapping mode to probe the topography of the sample with as little as possible tip-sample interaction. The cantilever was excited to oscillate, tip-sample contact only took place at the lower turning points of each oscillation. To obtain a topographic image of the sample area, the sample was moved by the x-y-piezoelectric stage and scanned line by line. At the same time PL image of the same area was obtained.

Pressing mode (Figure 2.2.3 c): The tip was positioned above a desired location and a force-distance-curve was carried out. Here, the deflection of the cantilever (which can be converted into the force) is recorded as a function of the vertical position (z) of the tip above the sample. The cantilever approaches the sample until a pre-set repulsive force is reached. This maximum force was held constant over a user defined time interval ranging from 10 to 1000 seconds. Forces from 2 nN to 200 nN where applied. PL could be monitored simultaneously from the area centered in the tip position and the diameter equal to the size of the confocal point spread function (PSF) (430 nm in our case) with time resolution of 0.5 ms.

Scratching mode (Figure 2.2.3d). To scratch the sample, the AFM was used in the imaging-contact mode, however only one line was scanned. The setpoint of the cantilever deflection (respectively the force) was set high enough, to achieve irreversible sample deformation. The force was held constant during the whole cutting process (one-dimensional scanning). Forces from 40 nN to 500 nN where applied. In some experiments PL intensity was recorded from the tip location during the scratching process with 50 ms time resolution. In other experiments, PL images of the whole crystal were recorded by sample scanning after the scratching process was completed. These procedures took some time which, as the reader will see later, will be important for the result interpretation.

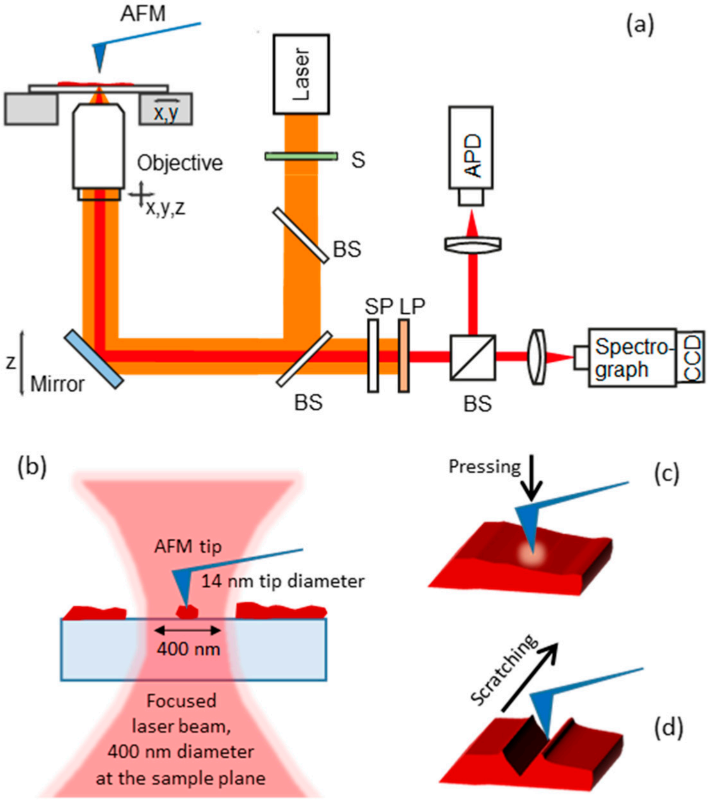

Figure 2.2.3. (a) Simplified sketch of the experimental setup consisting of a home built confocal luminescence microscope and a commercial atomic force microscope (AFM). S - shutter, BS - beamsplitter, SP - shortpass filter, LP - longpass filter, APD - Avalanche Photodiode, CCD - Charged Coupled Device. **(b)** Relation between the excitation spot size (400 nm), size of the perovskite crystals (from tens of nm to tens of micrometers) and the tip diameter (7 nm). **(c)** – Scratching of the sample with the AFM tip. **(d)** – Applying local pressure by the AFM tip. (Figures were edited by IGS)

2.2.4 Low temperature cryostat

To control the temperature of the local environment surrounding to the OMH perovskite, a cryostat (Jains ST-500 continuous flow cryostat) was used as sample chamber as shown in Figure 2.2.4. The sample was glued in the cold finger of the cryostat. Then, the sample chamber was vacuumed by an external air pump. Next, the cryostat was mounted on the top of the microscope so the sample was reached by the objective lens through the transparent optical window. Next, the liquid nitrogen was introduced to cool down the system. To get the required temperature, an external temperature controller was connected to the cryostat to control the heater inside the cryostat. For example, when the temperature in the chamber is lower than the required value, the heater starts to heat the chamber to stabilize the temperature.

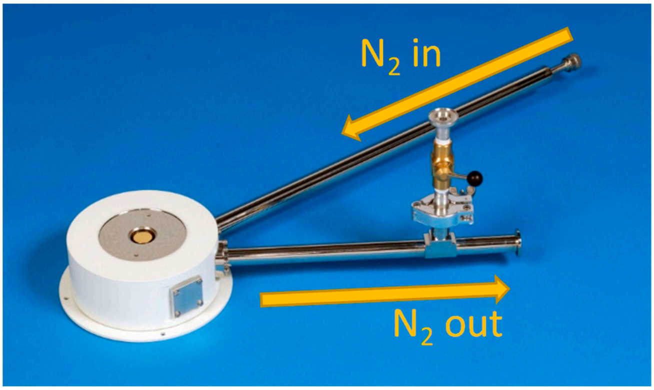

Figure 2.2.4 Image of cryostat used in this experiment.
(Image source: https://www.lakeshore.com/products/product-detail/janis/st-500-microscopy-cryostat)

2.3 Synthesis recipes of $MAPbI_3$ used in this study

2.3.1 Synthesis of concentrated $MAPbI_3$ films

The concentrated $MAPbI_3$ film was synthesized via one-step solution method. The $CH_3NH_3PbI_3$ ($MAPbI_3$, MA= $CH_3NH_3^+$) precursor solutions were prepared by dissolving 461 mg of PbI_2 (Sigma-Aldrich, 99%) and 159 mg of methylammonium iodide (Sigma-Aldrich, 98%) in 1.25 mL of DMF (Sigma-Aldrich, anhydrous) to make 0.8M $MAPbI_3$-DMF precursor solution. The solution was stirred for 2 h at 60 °C. A 100 μL of the precursor solution was dropped on a microscope coverslip (22 mm × 22 mm × 0.17 mm) at ambient conditions (≈50% humidity). The coverslip with precursor solution was treated by spin-casting (1460 rpm, 1 min) and annealed at 80 °C for 1 h. In this procedure, the solvent DMF could be replaced by GBL (gamma-Butyrolactone) as well.

2.3.2 Synthesis of low concentration $MAPbI_3$ films (individual crystals)

In this study, low concentration $MAPbI_3$ was prepared by a diluted $MAPbI_3$-GBL precursor solution. 0.8M $MAPbI_3$-GBL precursor solution was obtained by the similar procedure as described in Section 2.3.1. The obtained precursor solution was further diluted by 2000 times. Then the diluted precursor solution was dropped on the substrate followed by a thermal annealing at 80 °C for 20 min to get low concentration $MAPbI_3$ films.

2.3.3 Cleaning recipe of glass substrates and SiO_2/Si substrates in this study

The glass substrates used in this study were washed by 2% HellmanexIII water solution under 35 °C for 30 min with ultrasonic bath at first. Then the procedure was repeated by replacing HellmanexIII solutions with acetone and 2-propanol, respectively. Next, the 2-propanol was replaced by deionized water and repeated this procedure 2 times. Then the glass substrates were dried with nitrogen flux and transferred to the substrates holder. Finally, the dried substrates were placed under UV lamp for 30 min. For SiO_2/Si substrates, the cleaning procedures were the same, just skip the washing procedure by 2% HellmanexIII solution, as this solution could damage the SiO_2 layer on the substrates.

2.4 Some tips from sample synthesis experience

During my PhD studies, one of my main tasks was to prepare $MAPbI_3$ perovskite films or individual crystals for my own research projects and for my colleagues. The most common problem that I had was the low reproducibility of $MAPbI_3$ perovskite regarding their PL properties. In another words, the PL performance was be quite diverse even if the synthesis condition were the same. In this section, I would like to share some tips and my reflections about preparing $MAPbI_3$ perovskite samples.

2.4.1 Solvents selection

The effects of solvents to the PL of perovskite films have been discussed in many published studies. When preparing MAPbI3 films (high concentration samples) using DMF as the precursor solvent, I was always getting branch-like structures with a low surface coverage rate as shown in the insert in Figure 3.1.1 (b) in the next chapter. This branch structure was reported to be related to the DMF-MAPI intermediate phase.[[65]] When DMF was replaced by GBL, the typical branch structure from DMF was gone and I obtained sample consisted of many rather large (tens of micrometers) individual islands situated close to each other.

When preparing low concentrated $MAPbI_3$ films with separated individual crystals the goal was to obtain crystals of 100 – 1000 nm in size separated by several micrometers from each other. This was needed to observed them individually using the PL microscope. DMF and DMSO were selected as solvents in the beginning. However, only very large (about 20 to 100 micrometers) crystals were formed. In order to prepare smaller crystals, I used a mixture of DMF and DMSO, which was successful and this samples were studied in Paper iii (see list of publications not included to the thesis, page iii). However, this synthesis process was complicated as another cover glass was used to cover the top of the glass substrate with precursor solution to form a "sandwich" structure. Finally, GBL was selected and proved to be a good solvent for preparing individual $MAPbI_3$ crystals.

2.4.2 Substrates selection

In my work I used SiO_2/Si substrates and microscope cover glasses for preparing perovskites samples. Similar washing procedure was always used as described in Section 2.3.3. The only difference was that the SiO_2/Si was not treated with Hellmanex III solution in the beginning as it may damage SiO_2 layer. When preparing high concentration perovskite films (with large surface coverage), the difference was negligible. However, when preparing low concentrated $MAPbI_3$ films, the PLQY of individual perovskite crystals on SiO_2/Si was always lower than that on glass substrate, even when all other conditions were the same. We were not able to explain why this was happening.

2.4.3 Lab condition (humidity)

As we did not have a glove box in our chemistry lab, all the sample preparations were carried out under ambient air inside a fume hood. When I prepared samples in January or February (wintertime in Sweden), the PLQY of samples was usually higher and PL decay longer than for the samples prepared in June or July (summertime in Sweden). The average humidity in the chemistry lab varied from 30 % in cold winter days up to 60% or even more during summertime. Our feeling at that the humidity in the chemistry lab is a very important factor for the synthesis process and definitely influence the properties of the final perovskite semiconductor.

Chapter 3 Results and Discussion

In this chapter, we will present some results to show the PL of OMH perovskite samples under different local environment. The impact of the environment such as humidity, electric field, local pressure and temperature to the PL performance of OMH perovskite crystals or films will be discussed.

3.1 Paper I: Effects of humidity on the room-temperature crystallization of $MAPbI_3$ perovskite films

In this study, the home-made humidity controller described in section 2.2.1 was used to adjust the humidity of perovskite samples. Figure 3.1.1 (a) shows the time evolution of light transmission micrographs of the precursor films exposed to N_2 under different humidity level at room temperature. It can be observed that the sample remained transparent in dry N_2 (0% humidity) with leaf-like structure even after 1 h. When the humidity was higher (35% to 63% humidity), further evolution of the film was occurred as black phase was formed with branch structure (typical structure because of PbI_2). When the humidity is relatively high (>80%), black phase was formed in the beginning and then it turned to transparent again with changed orientation as marked by blue and yellow line. The transmission image of a reference (REF) sample formed by normal thermal annealing was inserted in Figure 3.1.1(b) in which black phase was observed.

The UV-VIS absorption spectra of reference sample, sample in dry N_2 after 3 and 60 min was presented in Figure 3.1.1 (b), in which no absorption in visible range was observed in the sample after conversion in dry N_2 for 3 min. Then it was increased in visible range after 60 min in dry N_2 but it is still weaker compared with reference as marked by black line. Moreover, the absorption edge at 750 nm in red line indicates that some materials was converted to $MAPbI_3$ phase and the absorption feature at 450 nm in 3 and 60 min indicated that the structure also contain lead-halide-solvent phase.

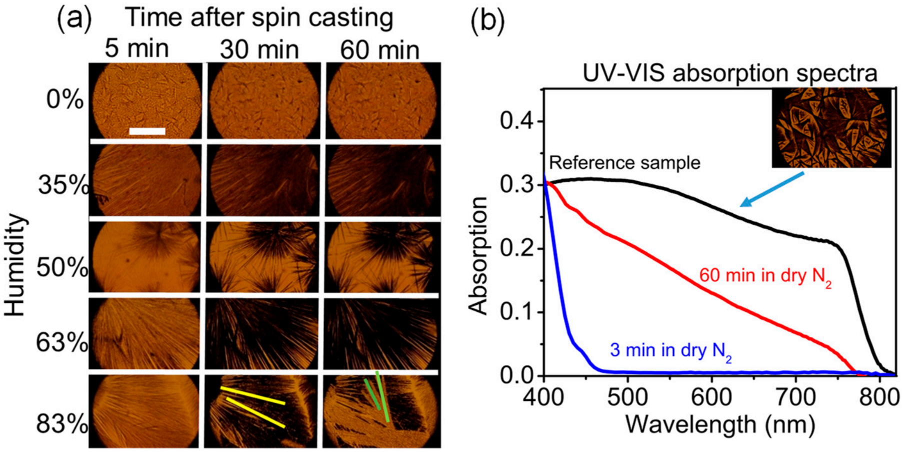

Figure 3.1.1. (a) Time evolution of light transmission micrographs of the precursor films exposed to nitrogen gas of different humidity. The scale bar is 200 µm. Yellow and green lines show the crystal growth directions of the perovskite (black phase) and transparent (hydrated perovskite) crystals for 83% humidity case. **(b)** The UV-VIS absorption of the reference (REF) sample, sample in dry nitrogen atmosphere after 3 and 60 min of conversion at room temperature. Inset - transmission micrograph of the reference sample.

The PL spectra of the sample from 5 min and 60 min from 0%, 35% and 63% humidity were collected and fitted with Pseudo-Voigt model and the results are presented in Figure 3.1.2. The evolution of the material in dry N_2 was also indicated by the change of PL spectra shape from multiband shape (600-750 nm) to a red-peak domain shape. By comparing with fitting results, it can be concluded that the initial PL spectra contains several high-energy bands and a low-energy band. The low-energy band become the main peak in the end while other high-energy bands remained unchanged. When the humidity was increased, the low-energy bands was observed in the beginning but they disappear in the end. More detailed results can be found in attached Paper I.

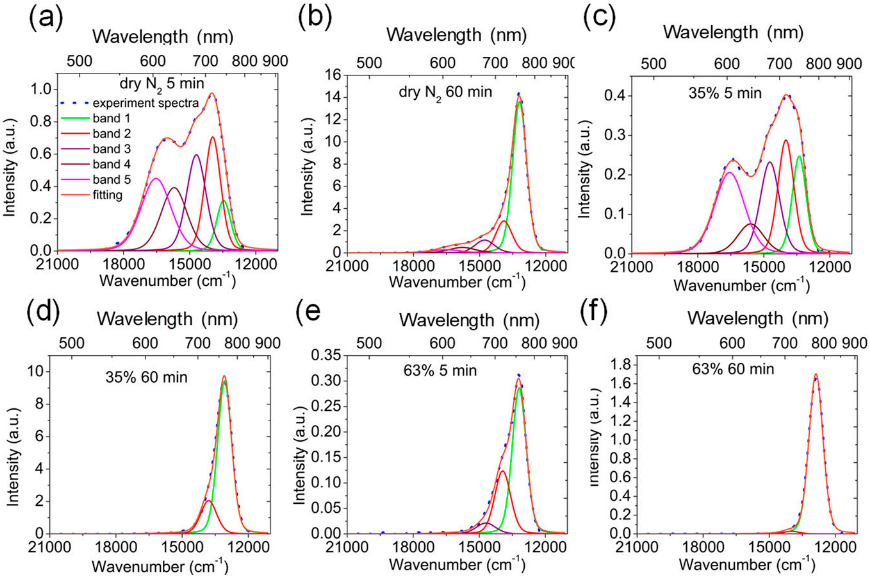

Figure 3.1.2 Pseudo-Voigt fitting of PL spectra measured at 5 min and 60 min during the sample evolution under different humidity at room temperature (the data indicated at the top of each spectrum).

Based on previous experimental results and some information from literature, the whole evolution process of $MAPbI_3$ film from liquid to solid phase under different humidity can be presented and illustrated by Figure 3.1.3. Take the sample in dry N_2 for example. The solvent perovskite phase ($MAPbI_3$ -DMF) was formed in the substrate in the beginning. Under room-temperature, even though most of the solvents was evaporated, there still exist lots of DMF molecule inside the structure because of the hydrogen bond between DMF and MA (MA-DMF). The formed MA-DMF does not fit the space of Pb-I octahedral, so the pure perovskite phase was not formed. Instead, the intermediate phase was formed which contains most of the low-absorption solvent-perovskite phase with some disordered bulk and some low dimensional perovskite phase embedded inside. This can be indicated by the appearance of blue-shifted high-energy bands as shown in the attached Paper I.

When the water molecule was introduced into the system, even though the low dimensional perovskite phase was formed in the beginning, water can remove the DMF molecule by either forming hydrogen bond with DMF (H_2O-DMF) or by replacing DMF in Pb-halide-structure because of stronger coordination to Pb. [74,77,100–102] Then the transparent intermediate phase was converted to 3D non-transparent perovskite phase. Higher humidity will lead to faster conversion rate. If the humidity is too high (>80%), we can get non-transparent perovskite very fast. However, the water will further interact with MA^+ by forming hydrogen bond (MA-H_2O). As the size of MA-H_2O is larger and it does not fit the space between Pb-I octahedral, the already-formed 3D perovskite structure collapsed again to form hydrate perovskite ($MAPbI_3$-H_2O) phase.

In conclusion, water can act as a catalyst to help the crystallization of $MAPbI_3$ from precursor solution in room temperature by removing residual solvent molecule. However, high humidity environment will lead to the recrystallization of non-transparent perovskite film to transparent hydrate phase.

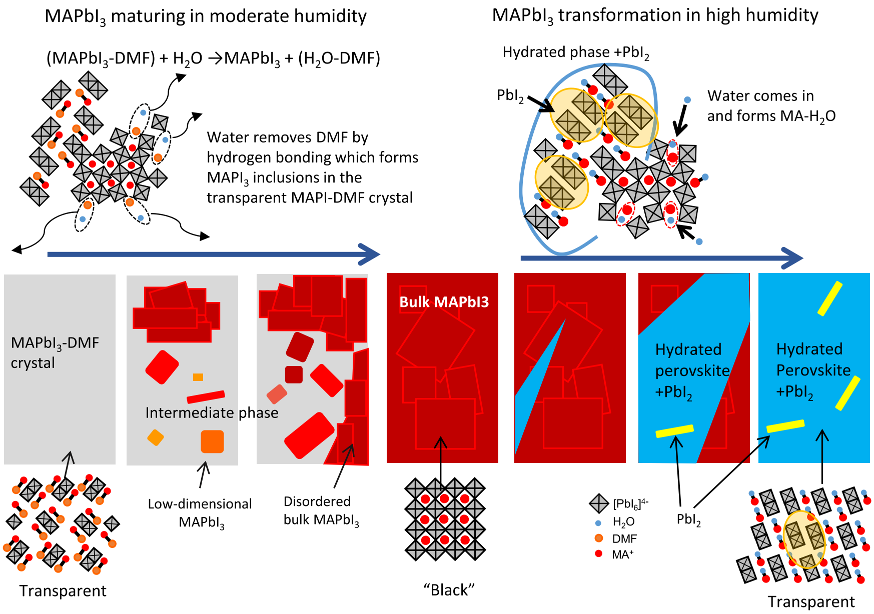

Figure 3.1.3 Cartoon illustrating our view on the room-temperature transformation of the perovskite precursor and final material at different conditions. It is based on the experimental observation of the film's transparency, PL intensity and spectra, visible film crystallinity, literature data about the intermediate stages, and the origin of the blue-shifted PL as luminescence of low-dimensional perovskite inclusions proposed here.

The room-temperature transformation of the perovskite DMF precursor film prepared from PbI_2 and MAI via intermediate DMF-$MAPbI_3$ phase was studied by PL micro-spectroscopy and light transmission imaging as a function of ambient humidity. We found an intermediate phase that possesses an appreciable PL with a broad multiband spectrum ranging from 600 to 760 nm, blue shifted from the expected PL peak of pure $MAPbI_3$ (760 nm). We propose that the blue-shifted PL comes from perovskite nanocrystals and other low-dimensional perovskite structures of different sizes present in the film. We suggest that water works as a catalyst helping to remove the residual DMF solvent from the film to accelerate the transformation to the perovskite structure. However, a prolonged exposure to water at high humidity (>80%) conditions leads to the recrystallization of the initially formed perovskite film to a transparent hydrated perovskite phase.

3.2 Paper II: Effects of external electric field on the PL of $MAPbBr_3$ perovskite crystals

As is mentioned in the previous part that understanding the effect of local electric field (EF) to the photoluminescence of OMH perovskite is quite important to the application of OMH based solar cell devices. To do this study, both $MAPbBr_3$ and $MAPbI_3$ crystals were deposited on the interdigitated electrode device as described in section 2.2.2. Then the device with perovskite sample were mounted on the microscope as shown in Figure 2.2.2 (a). In this chapter, we will only present the results from $MAPbBr_3$. More detailed information can be found in attached Paper II.

The PL and SEM images of device containing $MAPbBr_3$ nanocrystals are shown in Figure 3.2.1 (a) and (b), in which good correlation between PL and SEM results can be clearly observed and the crystals are located in the edge of the electrodes as shown in Figure 3.2.1 (b). Figure 3.2.1 (c) shows the COMSOL simulation of the EF intensity distribution between electrodes under 50V constant bias, in which strong EF amplitude was appeared in the edge of the electrodes (up to 4×10^5 V cm^{-1}).

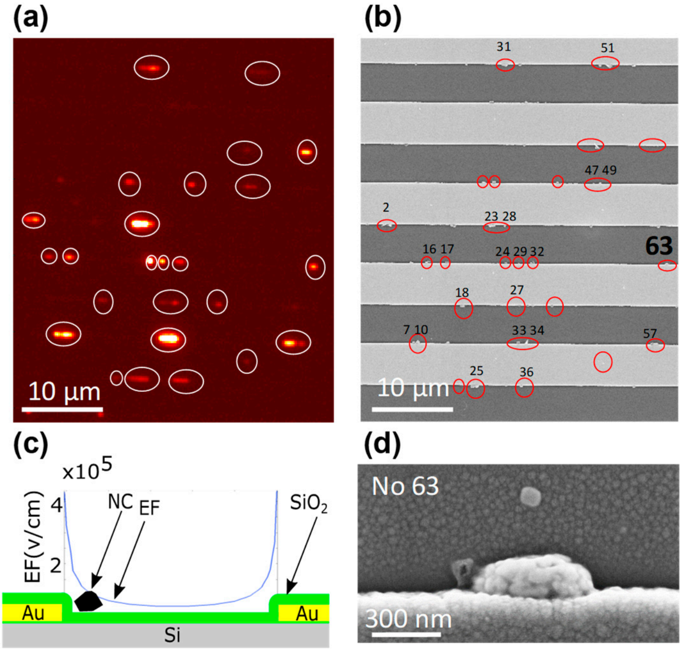

Figure 3.2.1 (a) PL image of $MAPbBr_3$ nano and microcrystals dispersed on the device with interdigitated electrodes with 5 µm gap. **(b)** SEM image of the same region of the device where electrodes and some crystals are visible, circles mark the same areas in (a) and (b), crystals are labeled by numbers. **(c)** The scheme of the device (not in scale), thicknesses of the layers: Au—210 nm, SiO_2—140 nm. The distribution of the EF over the electrode gap is calculated for 50 V constant voltage applied between neighboring electrodes using COMSOL simulation software. Close to the electrode edge, the EF reaches 4×10^5 V cm^{-1}. **(d)** SEM image of crystal no. 63 marked in **(b)**.

In this study, the 50 V constant EF and 50V 1 kHz alternating EF were applied on the device and the PL transients of several selected crystals during the EF loading/unloading process were recorded and the laser was kept on all the time. It can be observed that when constant EF was loaded, variable response behave was observed from different crystals as shown in attached Paper II. However, when the 50 V 1 kHz alternating EF was loaded on the device, almost all the crystals showed PL quenching immediately after switching on EF. When the alternating EF was removed, the PL recovered to the initial level at the time scale of minutes.

Furthermore, when the frequency of the alternating EF was fixed at 1 kHz and the bias voltage of alternating EF was swept from ±10 V to ± 50 V as shown in Figure 3.2.2 (a), it can be seen that the PL of an individual $MAPbBr_3$ nanocrystal was not quenched when the bias voltage was ±10 V. Then the quenching became well pronounced when the bias voltage was increased to ± 20V and completely quenched under further higher value. When the voltage was fixed at 50V while increasing the frequency from 1 Hz to 1 kHz, it can be observed that higher frequency induced stronger PL quenching with much slower recovery rate compared as shown in Figure 3.2.2 (b).

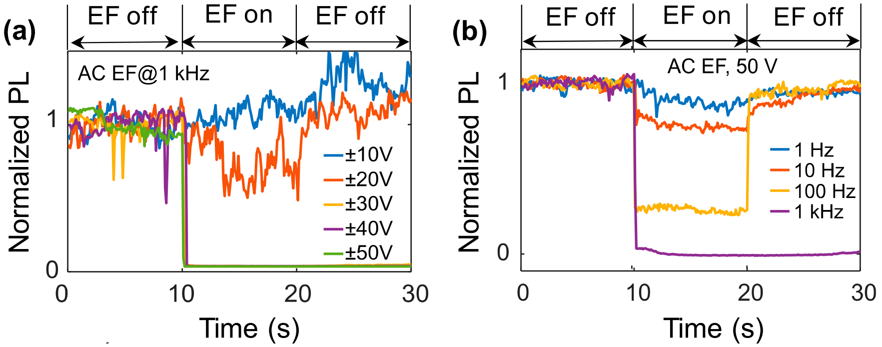

Figure 3.2.2 **(a)** Normalized PL intensity traces of an individual $MAPbBr_3$ crystal under 1 kHz alternating EF with different bias amplitude. **(b)** Normalized PL intensity traces of another individual $MAPbBr_3$ crystal (No. 63) under ±50 V alternating bias with different frequency. Switching of the EF is marked with blue dash line. The sample was irradiated by the laser over the whole measurement.

Now it was experimentally observed that the PL of $MAPbBr_3$ nanocrystals will be quenched under alternating bias. However, as the laser light was remained on during the whole process, the effect of light during the quenching and recovery process should not be ignored. Here, a set of control with “on” and “off” between EF and laser were carried and the results are shown in Figure 3.2.3.

The response of PL to the change of laser was first checked by switching laser while keep EF off during the measurement as shown in Figure 3.2.3 (a). An instantaneous response can be obtained, indicating that the sensitivity of the detector will not lead to the delayed PL response. Then the PL transients of crystal during switching on and off the EF with laser illumination all the time and the results are shown in Figure 3.2.3 (b), in which a PL quenching and slow PL recovery was presented. Next, the EF was added during the dark period and the PL transient was shown in Figure 3.2.3 (c) where a faster PL recovery can be observed. In the end, the effect of dark to the PL recovery rate was checked as shown in Figure 3.2.3 (d) in which the experiment was exactly the same as described in Figure 3.2.3 (b) in the beginning, then the EF and laser were switched off at same time. After 10 s, the laser was switched on again. It can be observed that the PL recovered even slower compared with case (b), which indicates that the laser may help the material to recover to the initial state.

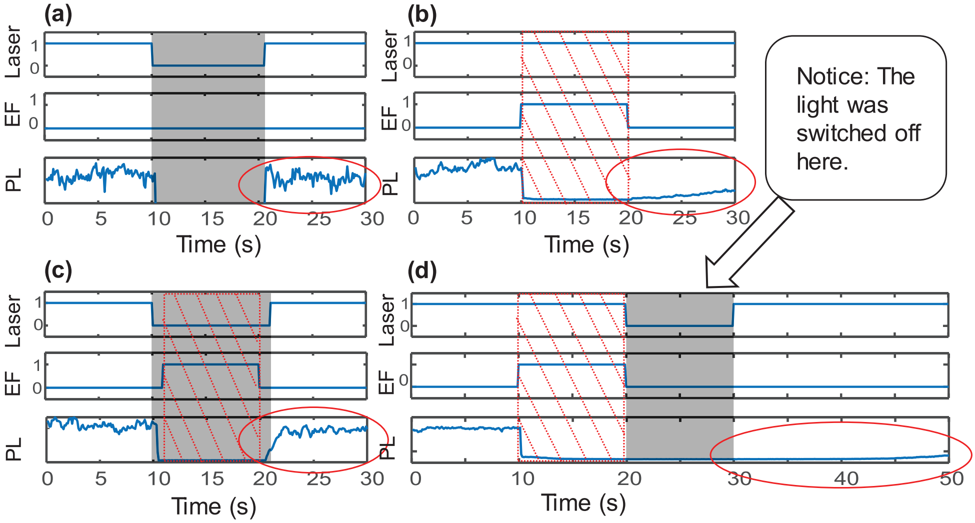

Figure 3.2.3 PL intensity transients of the individual $MAPbBr_3$ crystal (no. 63) under light irradiation and alternating bias (±50 V@1 kHz) applied in different combinations. **(a)** The laser was switched on and off without bias (dark period is shown by gray coloring). **(b)** The laser was always on while the EF was switched on and then off (red hatching). **(c)** EF was applied during the period when the laser was switched off. **(d)** The same experiment as in (b) but the laser was switched off for 10 s at the same time with switching off the EF. Compare the PL recovery kinetics in all graphs, marked by red ellipses.

In this study, the constant EF showed diverse effects to $MAPbBr_3$ crystals while the alternating EF quenched PL from almost all the crystals. In fact, when the EF (no matter constant or alternating EF) was attached on the crystal, the actual internal EF inside the crystal is weaker compared the external EF by a factor of dielectric constant ε.

For constant EF, the ε is about 1000 and it decreases by one or two order when increasing the frequency (1 kHz) of the alternating EF. Hence, the internal EF under constant bias is much weaker than under alternating EF. In this case, the constant EF can only change a little on the pre-existing NR centers and charge accumulation on grain boundaries as well as surfaces but not create new NR centers. For different crystals, the morphology as well as the grain boundary are quite different from each other, so the “pre-conditions” are quite different, this can explain the diverse PL response from different crystals.

Alternating EF, however, can induce EF with orders of magnitude higher in inside the crystals in comparison to the constant EF due to a lower dielectric constant for alternating EF (1 kHz). This alternating EF is able to create NR recombination centers by promoting ion migration. In all experiments, the rate of creation and annihilation of the PL quenching centers showed clear dependence on the light illumination conditions as expected for an ion-migration-induced process. The whole observations fit the qualitative picture where the external EF determines the balance between the radiative and NR recombination (equilibrium conditions) while light illumination influences the speed the equilibrium is reached. Besides fundamental interest, our results can be useful in application of MHP as optoelectronic switches including neuromorphic optoelectronics where responses with memory/delay can be of an advantage.

In conclusion, we studied the effect of electric field (EF) on the PL of sub-micrometer polycrystals of $MAPbX_3$(X = Br, I) perovskite. It was found that a constant EF shows very individual effects on PL of $MAPbBr_3$ polycrystals ranging from PL quenching to PL enhancement and from an immediate to a delayed response. At the same time, alternating EF (10-1000Hz) was found to reversibly quench PL of all studied crystals for both perovskite materials. We propose that alternating EF has such a clear effect first of all due to the orders of magnitude higher EF inside the crystals in comparison to the constant EF due to a lower dielectric constant for alternating EF in comparison with the static conditions. We propose that this alternating EF is able to create NR recombination centres by promoting ion migration. The constant field, although much weaker, acts for a long time uni-directionally, which eventually can change the status of already existing NR centres and states at the surfaces and grain boundaries. This can lead to either changes of PL (quenching or enhancement) depending on the initial conditions in the crystal. In all experiments, the rate of creation and annihilation of the PL quenching centres showed clear dependence on the light illumination conditions as expected for an ion-migration-induced process. The whole observations fit the qualitative picture where the external EF determines the balance between the radiative and NR recombination (equilibrium conditions) while light illumination influences the speed the equilibrium is reached. Besides fundamental interest, our results can be useful in application of OMH perovskite as optoelectronic switches including neuromorphic optoelectronics where responses with memory/delay can be of an advantage

3.3 Paper III: Effects of local pressure and structural damage on the PL of MAPbI$_3$ nanocrystals

It has been mentioned in chapter 1 that local pressure may affect the PL of MAPbI$_3$ perovskite nanocrystals. In this study, we used an AFM tip to perform some nano-scale manipulation and a confocal PL microscopy to study the PL of MAPbI$_3$ at the same time. The setup is shown in section 2.2.3. The top surface of the sample which is mechanically manipulated, while PL is excited and collected from the glass side of the sample (bottom side of the sample)

Panels a0 and b0 in Fig.3.3.1 show AFM and PL images of a MAPbI$_3$ microcrystal of 30 -100 nm thickness and about 1000 nm in diameter placed into argon atmosphere. After acquiring these initial images, the crystal was scratched by moving the sample along Y-axis (vertical axis in the figure) with the tip inserted into the crystal. After each vertical scratch which is clearly visible at the AFM images (panels a1, a2 and a3), PL image was recoded (panels b1, b2 ad b3). Surprisingly, none of these drastic manipulations of the crystal resulted to any PL intensity quenching of this crystal. Even slight increase of the total PL is observed as shown in Fig. 3.3.1c. However, it may take 5 minutes to finish scanning after each scratching, while no damage on PL intensity was observed even though strong mechanical damage was observed.

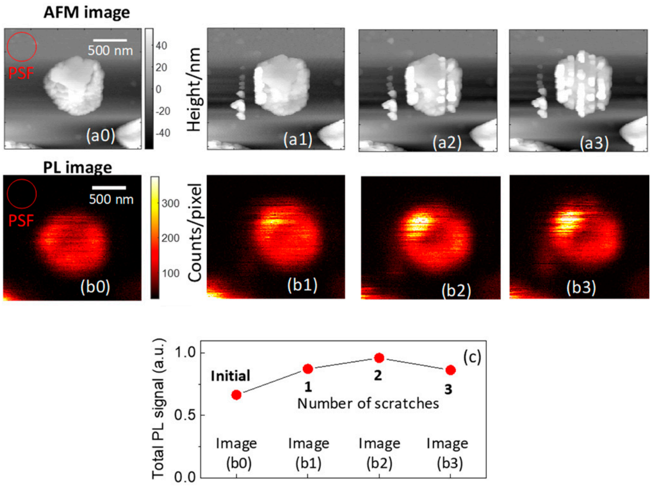

Figure 3.3.1. AFM and PL images of a MAPbI$_3$ crystal before **(a0, b0)**, after 1st **(a1,b1)**, 2nd **(a2,a2)** and 3rd **(a3,b3)** scratching of its surface, the scale bar is 500 nm. **(c)** The integrated PL counts obtained from the corresponding PL images. The sample was in argon atmosphere.(Figures are edited by IGS)

Realizing that PL could potentially already recover during the delay from the mechanical damage and PL detection, we recorded PL transients while grooving crystals (Fig. 3.3.2). Note that the objective of the confocal microscope was aligned with the AFM tip and the PL was detected from a region is about 430 nm in diameter corresponding to the confocal point spread function (PFS). The start time (the tip was inserted in the crystal) and end time (the tip was removed from the crystal) of the scratching process are marked by the red box in Fig. 3.3.2 c. Before scratching of the crystal, its PL intensity shows random blinking. Within a few seconds after inserting the tip and starting scratching, the PL becomes heavily quenched. After removing the tip, the PL intensity stays at the low level and slowly recovers to the initial level after approximately 120 s. Thus, we conclude that recovery of PL at the time scale of minutes after ending of the mechanical treatment is the reason why no changes of PL are observed in the experiment shown in Fig. 3.3.1. We also recorded PL spectra of the same crystal during the scratching process (Fig. 3.3.2 d) and observed no detectable spectral changes between the initial, final and partially recovered PL.

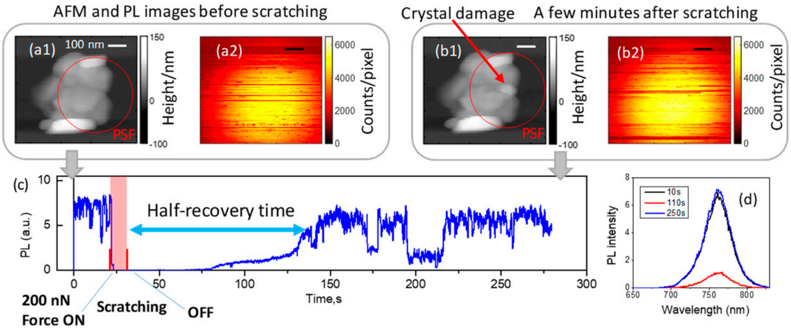

Figure 3.3.2 AFM and PL image of a $MAPbI_3$ nanocrystal before **(a1, a2)** and after **(b1,b2)** nano-scratching. Note the change of the topology due to scratching shown by arrow in **(b1)**. The scale bar is 100 nm, red circle is the PFS. **(c)** PL transient from during the whole experiment where the signal was collected without scanning of the sample stage from the area limited by the PSF of the microscope showed by the red circle in a1 and b1. The times of application and removing the force (200 nN) are marked with red ticks. **(d)** PL spectra of the crystal obtained at different times showing absence of spectral shifts. (Figures are edited by IGS)

It was proved from the previous experiment that scratching can induce temporary PL quenching, while local pressure or crystal strain might be created at the same time. So here comes a question: Can a local ressure generate such temporary PL quenching without structural damage? To answer this question, an AFM tip was used to press against crystal with a substantially smaller force (from 5 to 120 nN creating about 100 MPa to 3 GPa) and the pressure was hold about 10 s and the results are presented in Figure 3.3.3. Similar temporary PL quenching was observed, while there were some differences: i) scratching usually quenches PL to a lower level than pressing, ii) while the effect of scratching on PL is very fast and usually beyond our time resolution (50 ms), applying of pressure leads to a clearly resolved PL decline at the time scale about 1 s. It can also be obsereved that stronger force leads to faster PL decline in many crystals and PL recovery can even happen without light illumination. More information are presented in attached Paper III.

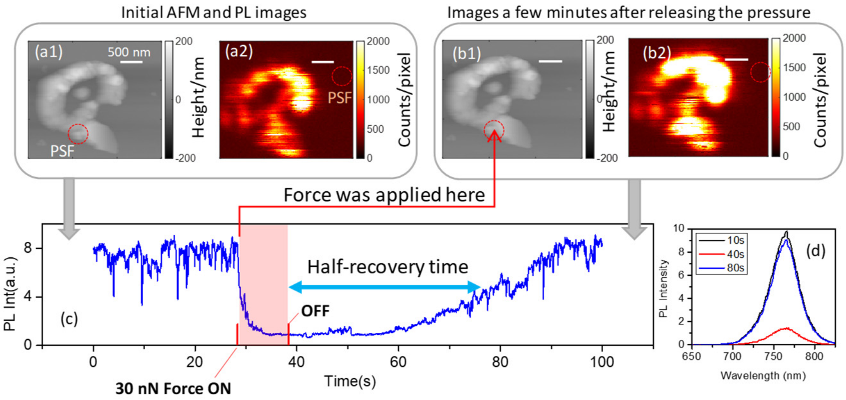

Figure 3.3.3. AFM topography and confocal PL images a of $MAPbI_3$ nanocrystal before **(a1,a2)** and several minutes after releasing the pressure. The scale bar is 500 nm. The point where the pressure was applied is shown by an arrow in **(b1)**. **(c)** PL signal measured in the confocal regime from the point of the force application. The signal was integrated over the area covered by PSF, which diameter is shown by the red circle (420 nm). The times when the force (30 nN) was applied and released are marked by the vertical red ticks. **(d)** PL spectra of the crystal obtained at different times showing absence of spectral shifts. (Figures are edited by IGS)

In this study, the AFM tip was used to manipulate on the surface of the perovskite while the PL was detected from the bottom. Nevertheless, it did not prevent us to see the tip-induced PL quenching. This is because the charge diffusion length in $MAPbI_3$ is at least several hundreds of nanometers [[26]] making the local defected area accessible over this length. We also chose 640 nm excitation light due to its penetration depth (1/e attenuation) as large as 200 nm for the $MAPbI_3$ material,[[26]] which is larger than the thickness of the studied crystals.

Quenching by local pressing and/or mechanical damage nicely illustrates the ability of a local area containing defects (the contact area of the tip is about 50 nm^2 only) to influence the charge dynamics of whole crystal of several hundreds of nanometers in size. If the crystal is large, we can definitely say that its area of at least the size of confocal PSF (430 nm) is affected.

It is well-known that $MAPbI_3$ crystals of similar sizes demonstrate so-called PL blinking effect, which is explained by temporal formation of a very strong metastable quencher (supertrap) which can non-radiatively recombine the majority of photogenetated charges from crystals as large as charge diffusion length in the material.[[103,104]] In our experiments we also created a local defected area which captures charge carriers when they pass by in their diffusion leading to NR charge recombination. The creation of the NR centers by the AFM tip is fully controlled while appearance of the super-traps is stochastic. It is also interesting to see that mechanically created NR centers are also not stable, as well as the spontaneously occurring super-traps. All these allows us to speculate that probably there is a connection between the metastable NR centers causing random PL blinking (super-traps) and mechanically induced NR centers.

We are not able to say how many efficient NR centers are created by pressing or scratching. However, based on the fact that the PL increasing during the recovery process is usually quite smooth and gradual, we suggest that in most of cases the number of NR centers created by pressing or scratching is large. Most probably there were many NR centers, but having only one of the in the crystal was already enough to quench PL substantially, that is why during the recovery the strongest effect on the observed PL is observed when the last NR center is removed appearing as a sudden jump of PL intensity up. [41]

Our experiments clearly demonstrate that the thermodynamically stable state of the $MAPbI_3$ crystals is the state with high PL intensity level. It means that even that quenching of PL by 10-100 times or even more can be easily induced by mechanical deformation/damaging of the material at the nano scale, it is only temporal. This is observed not only in this study but also under external EF effect. This property is definitely beneficial for applications of these materials. The recovering ability is strong and in some cases its leads to self-recovery even under continuously applied force.

The observed behaviour of the material reminds that of a living tissue which is trying to heal the damage and adapt for the new environmental conditions (pressure). Another, probably much closer analogy is a very viscous liquid or a tar. Tar can be cut in pieces; it is a hard material where a strain can be also created by pressing. However, after a while (hours, days) all these defects either completely disappear or the material will adopt to their presence due to its fluidity. We propose that fluidity of $MAPbI_3$ is the main reason for the self-recovery effect.

In conclusion, we demonstrated and studied the self-healing properties of $MAPbI_3$ perovskite by applying atomic force microscope (AFM) to make nano-scale damage using its tip and confocal PL microscope to study the PL properties during the mechanical manipulation. The fast PL quenching and slow PL recovery of $MAPbI_3$ perovskite was observed under local pressing/mechanical damage. One possible explanation might be that the nano-scale damage induced by AFM tip may create lots of metastable NR centers in $MAPbI_3$ nanocrystals. Besides, $MAPbI_3$ nanocrystals might either recover to the initial state or reach to a new balance state even when the surrounding condition is changed due to is low barrier energy for creation and annihilation of defects. At the same time, the crystal strain induced by the AFM tip might also induce NR centers.

3.4 Paper IV: Effects of low temperature on the PL of $MAPbI_3$ films.

It has been mentioned in Chapter 1 that defects in OMH perovskite film are the main reason for NR recombination that “steal” most of the incident energy and defects are mainly formed during the crystallization process. Although lots of efforts have been spent on improving chemical synthesis process to reduce amount of defect to get higher PCE, understanding the nature of defects is still a tough task. However, defect-related emission at cryogenic conditions provides an independent approach to study defect states. At room temperature, emission from such defects is hard to detect. Indeed, we can see them only indirectly via their influence on the observables like band-edge PLQY, time-resolved PL dynamics, charge mobility, and so on. While at low temperature we can see and study the emission of some of the defect states themselves.

In this study, $MAPbI_3$ films were synthesized with two different methods. The sample named “MAPI” were synthesized by the general one-step method described in Chapter 2.3.1 with DMF as solvent at ambient environment. The sample “MAPIC” was synthesized in a glovebox under a nitrogen atmosphere using a commercial perovskite precursor ink that has been optimized for processing of perovskite-based photovoltaic devices with power conversion efficiencies of 12%.

Microscopy and PL spectral characterization of both films are presented in Figure 3.4.1, where MAPIC film shows larger grain size with better surface coverage, longer PL decay kinetics as well as higher PLQY than MAPI film.

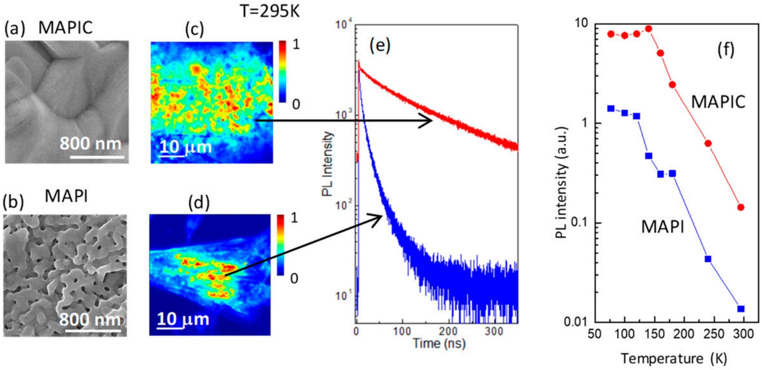

Figure 3.4.1 Microscopy and PL spectral characterization of the MAPIC and MAPI films: **(a and b)** SEM images, **(c and d)** PL images 295 K (note that the laser excitation spot has a Gaussian-like shape with the maximum intensity in the middle of the image), **(e)** PL decays at 295 K (excitation power density 40 nJ/cm^2/pulse, repetition rate 2.5 MHz, charge carrier concentration ca. 10^{15} cm^{-3}), and **(f)** temperature dependence of the integrated PL intensity. Observe the approximately 10 times higher PL quantum yield of the MAPIC film.

At room temperature (295 K), PL spectra of both films are the same with emission peak located at 775 nm (tetragonal phase) as shown in Figure 3.4.2 (a). However, when the temperature is lower than 120K, the PL spectra of both films are quite different. For MAPIC sample, the PL spectra shows an emission peak located at 750 nm (orthorhombic phase) with a broad low-energy tail which is pure band-edge emission. In contrast, the PL spectra of MAPI sample is dominated by a broad-band low-energy emission in the range of 770-950 nm which is almost pure defect emission.

The obtained PL spectra can be divided into three spectral regions as marked in Figure 3.4.2 (b). Here, OP region is attributed to the orthorhombic phase, LE1 is the tetragonal inclusions due to incomplete phase transition and LE2 is completely assigned to radiative recombination of charge carriers trapped in defect. In order to obtain the distribution of each components in perovskite film, three emission filters corresponding to the spectral region mentioned above were placed in front of the CCD camera to get the PL image of the same area. They are a 760 nm short-pass filter for OP region, a 770 nm long-pass filter to detect all LE1+LE2 region and an 820 nm long-pass filter to detect only the LE2 spectral range. Transmission spectra of these filters together with the PL spectrum of the investigated films at 77 K are presented in Figure 5.4.2 a. To separate the contribution of the emission of the LE1 region, we subtracted the signal detected for each pixel with the 820 nm long-pass filter (LE2 region) from that measured with the 770 nm long-pass filter (LE1+LE2 region).

For the MAPI sample, the PL image of the orthorhombic phase (OP region) shows spatially separated individual regions while most of the image remains dim. It can be indicated that the band-edge PL is strongly quenched in most of the crystals while in some part the amount of NR centers is quite small. Besides, PL maps of the tetragonal inclusions (LE1 region) and defects (LE2 region) show much more homogeneous intensity distribution all over the film. However, the optimized MAPIC film shows the opposite picture: the PL image of the orthorhombic phase (OP) consists of numerous rather large emitting domains extending over several micrometers, while the sub-bandgap emission (LE1 and LE2 regions) shows distributed point like emitting sites.

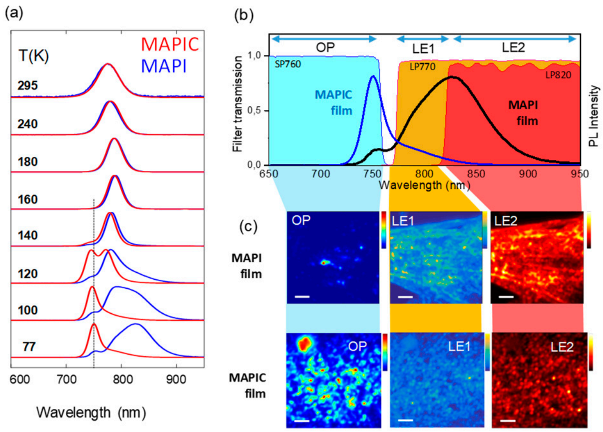

Figure 3.4.2 (a) PL spectra evaluation of the MAPI and MAPIC films at 77 K. **(b)** PL spectra together with the transmission spectra of the emission filters (SP760, LP770, and LP820) used for spectral imaging. Spectral regions OP, LE1, and LE2 are defined in the figure. (c) Spectrally filtered PL images of three different PL components at 77 K (scale bar, 5 μm). Intensity in all images is normalized according to the color schemes. Note a clear presence of individual emitting sites in the MAPIC LE2 image.

Up to now, it can be concluded from the previous results that the more traps the $MAPbI_3$ film has (result in lower band-edge PL intensity), the stronger defect emission intensity at lower temperature. However, the relationship between the defect which shows emission at low temperature and the defect related to NR recombination at room temperature is still missing.

As discussed in Chapter 1 that there exist "shallow" traps and "deep" traps in $MAPbI_3$ perovskite, as shown in Figure 3.4.3 (a). Generally speaking, "shallow" traps do not act as NR recombination center because of a much lower capture cross section for the opposite charge. Only the "deep" traps can act as NR recombination centers (process 6 + 7, capture and recombination of charges via a NR center) leads to NR recombination and thus determines the PLQY of the material. A strong NR center should provide efficient sequential trapping of both charges, or, in other words, provide a ladder of states for an electron to relax down to the valence band. This can be achieved by having a state in the middle of the bandgap (Shockley−Read− Hall recombination) or by a defect complex providing effective electron and hole trapping states on the same site or in the near spatial vicinity. Because we do not know the actual nature of the NR center, it is shown as a gray box in the schematic. This picture predicts that there should be no correlation between the NR recombination (processes 6 + 7) and low- temperature sub-bandgap emission (process 5) because the two processes are related to different sub-bandgap species.

In order to confirm this hypothesis experimentally, the spatial PL distribution of both $MAPbI_3$ films at 77 K and 295 K was analysed pixel by pixel in CCD image with 1 μm spatial resolution. Figure 3.4.3 (b) shows the scatter plots where the abscissa is proportional to PLQY and the ordinate to the defect emission intensity. By comparing the PL of each location of the sample at 295 K with exactly the same location at 77 K, we essentially probe thousands of samples with varied defect concentration due to the sample inhomogeneity. It can be observed that no correlation between PLQY and defect emission is observed as illustrated by a yellow horizontal line for MAPI (a fairly constant defect emission fraction independent of a broadly distributed PLQY) and a yellow circle for MAPIC (absence of any correlation between the two parameters which vary substantially). However, it can be indicated from the previous results that if the crystal has more NR centers, it should have more shallow trap numbers at the same time.

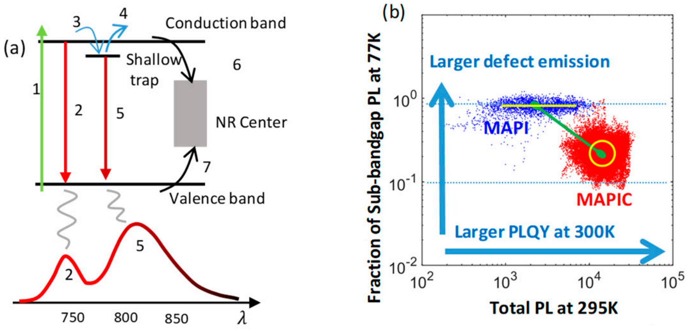

Figure 3.4.3(a) General scheme of the relaxation processes in semiconductors: 1, absorption; 2, band-edge PL; 3, trapping on the shallow trap; 4, temperature activation to the band; 5, sub-bandgap PL; 6, capturing an electron by a nonradiative (NR) center; 7, nonradiative recombination by capturing a hole. **(b)** Correlation between the contribution of the sub-bandgap PL to the total PL at 77 K and PL intensity at room temperature. Each data point corresponds to one pixel of the CCD camera, and the optical resolution is approximately 4 pixels (1 μm). Blue dots, simple MAPI film; red dots, optimized MAPIC film. The yellow dashed line shows the correlation between the defect emission at 77 K and PLQY of the sample. This correlation, however, is not visible within each sample.

In this study, we studied the PL of two $MAPbI_3$ films synthesized from different methods under low temperature, it appears that within each sample the local presence of more NR centers does not lead to a higher number of shallow defect states emitting at low temperature. This means that NR centers must have a different nature than the shallow defect states and may be even spatially situated in different locations at the nano and micro scales as indicated by PL multispectral imaging. However, there must be an indirect connection between the NR centers and the shallow traps, and this connection must be specific to the preparation procedure. Therefore, we must conclude that formation of the both defect types is promoted or suppressed by the sample preparation conditions. For the example of the two preparation methods, we see that if the method leads to a higher concentration of NR centers, it also creates a higher concentration of the defects yielding PL emission at low temperature. In other words, the chemical processes behind the formation of both types of defects must be connected, although NR centers and the shallow states probably form at different locations (e.g., surface versus bulk) of the material.

Chapter 4 Conclusions

In this thesis, I presented studies of PL properties of $MAPbI_3$ and $MAPbBr_3$ perovskite semiconductors under influence of several external environment factors such as the presence of water in the atmosphere, electric field, pressure and mechanical damage as well as temperature characterized by the PL microscopy and spectroscopy.

All studies presented in the thesis we are dealing with defects and their transformations in OMH perovskites. First of all, the formation of the perovskite from precursor solution is a complicated process which may leave the final material to contain various types of defects and crystal structures as discussed in Section 3.1. We further showed using PL that shallow and deep defects states are formed in proportional concentrations, meaning that their formation must have some common chemistry (Section 3.4). Although we are able to create intentionally ("by hand") lots of defects and quench PL by applying electric field or pressure or by simply cracking or cutting the semiconductor at nanoscale, studied perovskites were always able to recover their properties and come back to the initial state. We interpret this fantastic self-healing property as the result of the soft and dynamic crystal structure of the perovskites allowing for ion migration and spontaneous rebuilding of the initial structures from the available atoms (Section 3.2 and 3.3).

The motivation for me to do all these studies was to contribute to answering the question why OMH perovskites work so well for solar cells. I think that the self-healing property is one of the reasons. Hopefully further work in these directions will allow to shed light on the chemistry of the defect formation and healing and this is important for the long-term stability of OMH perovskite based solar cells. Even though there are still lots of mysterious things about perovskites, I think that this work helps to move forward and will be continued by other researches in the future.

Acknowledgements

Time is flying and I am growing up all the time. Now it's time to give a short summary and say goodbye to my PhD life in Lund University. During the past four and half years, I have learnt a lot both in science and life. A completely different environment, different lifestyle, a lot of unforgettable memories have made a difference in my life.

In the beginning, I should thank my PhD supervisor Prof. Ivan Scheblykin. He gives me a chance to come to study in Lund. I still remember the moment of Oct 20th in 2015, when I first wrote an email to him and ask for information about PhD position. Then we had hundreds of emails to discuss a solution for a question. I still remember he said he was 80% interested in me after first Skype meeting. Then we had hundreds of emails to get the answer for a testing problem. Actually it was my first time to have Skype meeting with foreign professor and I was so excited at that time. Then we fixed all the documents for CSC application in the beginning of 2016. Finally, I got CSC scholarship and came here. I have learnt a lot from him.

I also thank my vice supervisor Dr. Eva Unger. She is an expert in chemical synthesis and I got lots of help from her during my study. When I had a problem related to chemistry or synthesis, she was always my first option to ask.

I also thank all members from SMS group. Prof. Yuxi Tian, Prof. Ruiyun Chen, Dr. Aboma Merdasa, Dr. Alexander Dobrovolsky, Dr. Marina Gerhard, Dr. Daniela Täuber, Dr. Sudipta Seth, Dr. Aymen Yangui, Dr. Shraddha Rao, Dr. Chen Sun, Juanzi Shi, Boris Louis, Alexander Kiligaridis, Klara Suchan, Safi Zinedine. I am always confident during my study because I know you guys can always give me strong support. I learned a lot from you and I really enjoy working with you all. I still remember our group name "SMS" is "Sport Music Science" group. We had lots of group party and we played guitar together. We went to China and climbed the "Great Wall" together. We ran Lundaloppet together. We did lots of things together. All these things will stay in my memory forever.

I also received lots of support and help from other collaborators. Dr. Pavel Frantsuzov from Novosibirsk State University gave me strong theoretical supports during my research. I really enjoyed his "scientific story". And Prof. Thomas Basché, Marco Galle from Mainz University. They gave me a chance to get to know about the fantastic AFM-PL microscopy. And this setup can act as a strong tool to study more about perovskites and other materials.

During my PhD study, I also got lots of support from other people in Division of Chemical Physics. Prof. Tönu Pullerits, Prof. Arkady Yartsev, Prof. Ebbe Nordlander, Prof. Donatas Zigmantas, Dr. Pavel Chabera, Dr. Jens Uhlig and many other colleagues. Thank you all for helping me all the time and I really enjoyed discussing with all of you.

To my Chinese friend in Lund: 田玉玺，郑凯波，陈瑞云，张伟和苏晓俊，陈俊生，刘禹辰，姚泽涵，郭美沅，时娟孜，石琪，邹贤劭，李传帅，李勇，王政军，林炜铧，孙辰，吴凡，以及在这边交流过的张凤英，钟云倩，安锐，耿慧芳，周学宏，刘旸和刚刚来隆德的张伟（小），何燕梅，很高兴在过去的这么几年有你们的陪伴，见证了我从一个毛头小伙子变成了毛头老男人。在我遇到任何学术或者生活上的困难的时候，你们给了我巨大的帮助和支持。因为有你们，我的生活变得更加丰富多彩。希望你们未来的事业一帆风顺，十全十美，好运常在！还有很多的名字，在这里就不一一列举了，感激之情溢于言表！

我还要感谢我的家人，在我一个人背井离乡漂泊在外的时候，是你们给了我最大的支持。感谢你们三十年来对我的教育和付出。

最后我感谢中国国家留学基金委（CSC）给我提供了奖学金的支持，让我有这个机会在隆德大学学习。

There are still so many people which I would like to say “thank you” and hope you all be lucky in the future. If you are facing trouble, don’t forget my quote: Good food is good mood, life is beautiful, oh hahaha…

Best regards,
Jun Li (Bruce)

References

(1) Smith, W. Effect of Light on Selenium during the Passage of an Electric Current. *Nature* **1873**, *7* (173), 303. https://doi.org/10.1038/007303e0.

(2) Dobrovolsky, A.; Merdasa, A.; Li, J.; Hirselandt, K.; Unger, E. L.; Scheblykin, I. G. Relating Defect Luminescence and Nonradiative Charge Recombination in MAPbI<inf>3</Inf> Perovskite Films. *J. Phys. Chem. Lett.* **2020**, *11* (5). https://doi.org/10.1021/acs.jpclett.9b03878.

(3) Leguy, A. M. A.; Hu, Y.; Campoy-Quiles, M.; Alonso, M. I.; Weber, O. J.; Azarhoosh, P.; Van Schilfgaarde, M.; Weller, M. T.; Bein, T.; Nelson, J.; et al. Reversible Hydration of CH<inf>3</Inf>NH<inf>3</Inf>PbI<inf>3</Inf> in Films, Single Crystals, and Solar Cells. *Chem. Mater.* **2015**, *27* (9), 3397–3407. https://doi.org/10.1021/acs.chemmater.5b00660.

(4) Li, J.; Dobrovolsky, A.; Merdasa, A.; Unger, E. L.; Scheblykin, I. G. Luminescent Intermediates and Humidity-Dependent Room-Temperature Conversion of the MAPbI3 Perovskite Precursor. *ACS Omega* **2018**, *3* (10), 14494–14502. https://doi.org/10.1021/acsomega.8b01799.

(5) Shirayama, M.; Kato, M.; Miyadera, T.; Sugita, T.; Fujiseki, T.; Hara, S.; Kadowaki, H.; Murata, D.; Chikamatsu, M.; Fujiwara, H. Degradation Mechanism of CH3NH3PbI3perovskite Materials upon Exposure to Humid Air. *J. Appl. Phys.* **2016**, *119* (11). https://doi.org/10.1063/1.4943638.

(6) Song, Z.; Abate, A.; Watthage, S. C.; Liyanage, G. K.; Phillips, A. B.; Steiner, U.; Graetzel, M.; Heben, M. J. Perovskite Solar Cell Stability in Humid Air: Partially Reversible Phase Transitions in the PbI2-CH3NH3I-H2O System. *Adv. Energy Mater.* **2016**, *6* (19), 1–7. https://doi.org/10.1002/aenm.201600846.

(7) Acosta, M.; Novak, N.; Rojas, V.; Patel, S.; Vaish, R.; Koruza, J.; Rossetti, G. A.; Rödel, J. BaTiO3-Based Piezoelectrics: Fundamentals, Current Status, and Perspectives. *Appl. Phys. Rev.* **2017**, *4* (4). https://doi.org/10.1063/1.4990046.

(8) Zeches, R. J.; Rossell, M. D.; Zhang, J. X.; Hatt, A. J.; He, Q.; Yang, C.-H.; Kumar, A.; Wang, C. H.; Melville, A.; Adamo, C.; et al. Supporting Online Material for A Strain-Driven Morphotropic Phase Boundary in BiFeO 3. *Science (80-.).* **2009**, *324* (November), 63–67.

(9) Akihiro Kojima,† Kenjiro Teshima,‡ Yasuo Shirai, and T. M. Organometal Halide Perovskites as Visible- Light Sensitizers for Photovoltaic Cells. *J Am Chem Soc* **2009**, *131* (October), 6050–6051. https://doi.org/10.1021/ja809598r.

(10) Jacobsson, T. J.; Pazoki, M.; Hagfeldt, A.; Edvinsson, T. Goldschmidt Rules and Strontium Replacement in Lead Halogen Perovskite Solar Cells: Theory and Preliminary Experiments on CH3NH3SrI3. *J. Phys. Chem. C* **2015**, *119* (46), 25673–25683. https://doi.org/10.1021/acs.jpcc.5b06436.

(11) Tang, Z. K.; Zhu, Y. N.; Xu, Z. F.; Liu, L. M. Effect of Water on the Effective Goldschmidt Tolerance Factor and Photoelectric Conversion Efficiency of Organic-Inorganic Perovskite: Insights from First-Principles Calculations. *Phys. Chem. Chem. Phys.* **2017**, *19* (23), 14955–14960. https://doi.org/10.1039/c7cp02659e.

(12) Yin, W. J.; Shi, T.; Yan, Y. Unusual Defect Physics in CH3NH3PbI3 Perovskite Solar Cell Absorber. *Appl. Phys. Lett.* **2014**, *104* (6). https://doi.org/10.1063/1.4864778.

(13) Sutter-Fella, C. M.; Li, Y.; Amani, M.; Ager, J. W.; Toma, F. M.; Yablonovitch, E.; Sharp, I. D.; Javey, A. High Photoluminescence Quantum Yield in Band Gap Tunable Bromide Containing Mixed Halide Perovskites. *Nano Lett.* **2016**, *16* (1), 800–806. https://doi.org/10.1021/acs.nanolett.5b04884.

(14) Hoke, E. T.; Slotcavage, D. J.; Dohner, E. R.; Bowring, A. R.; Karunadasa, H. I.; McGehee, M. D. Reversible Photo-Induced Trap Formation in Mixed-Halide Hybrid Perovskites for Photovoltaics. *Chem. Sci.* **2015**, *6* (1), 613–617. https://doi.org/10.1039/c4sc03141e.

(15) Motti, S. G.; Meggiolaro, D.; Martani, S.; Sorrentino, R.; Barker, A. J.; De Angelis, F.; Petrozza, A. Defect Activity in Metal–Halide Perovskites. *Adv. Mater.* **2019**, *1901183*, 1–11. https://doi.org/10.1002/adma.201901183.

(16) Kim, J.; Lee, S. H.; Lee, J. H.; Hong, K. H. The Role of Intrinsic Defects in Methylammonium Lead Iodide Perovskite. *J. Phys. Chem. Lett.* **2014**, *5* (8), 1312–1317. https://doi.org/10.1021/jz500370k.

(17) Wang, T.; Daiber, B.; Frost, J. M.; Mann, S. A.; Garnett, E. C.; Walsh, A.; Ehrler, B. Indirect to Direct Bandgap Transition in Methylammonium Lead Halide Perovskite. *Energy Environ. Sci.* **2017**, *10* (2), 509–515. https://doi.org/10.1039/c6ee03474h.

(18) Ghosh, D.; Aziz, A.; Dawson, J. A.; Walker, A. B.; Islam, M. S. Putting the Squeeze on Lead Iodide Perovskites: Pressure-Induced Effects to Tune Their Structural and Optoelectronic Behavior. *Chem. Mater.* **2019**, *31* (11), 4063–4071. https://doi.org/10.1021/acs.chemmater.9b00648.

(19) Jiang, S.; Fang, Y.; Li, R.; Xiao, H.; Crowley, J.; Wang, C.; White, T. J.; Goddard, W. A.; Wang, Z.; Baikie, T.; et al. Pressure-Dependent Polymorphism and Band-Gap Tuning of Methylammonium Lead Iodide Perovskite. *Angew. Chemie - Int. Ed.* **2016**, *55* (22), 6540–6544. https://doi.org/10.1002/anie.201601788.

(20) Ehrenreich, H. Band Structure and Electron Transport of GaAs. *Phys. Rev.* **1960**, *120* (6), 1951–1963. https://doi.org/10.1103/PhysRev.120.1951.

(21) Fischetti, M. V.; Laux, S. E. Band Structure, Deformation Potentials, and Carrier Mobility in Strained Si Ge, and SiGe Alloys. *J. Appl. Phys.* **1996**, *80* (4), 2234–2252. https://doi.org/10.1063/1.363052.

(22) Anaya, M.; Galisteo-López, J. F.; Calvo, M. E.; Espinós, J. P.; Míguez, H. Origin of Light-Induced Photophysical Effects in Organic Metal Halide Perovskites in the Presence of Oxygen. *J. Phys. Chem. Lett.* **2018**, *9* (14), 3891–3896. https://doi.org/10.1021/acs.jpclett.8b01830.

(23) Gélvez-Rueda, M. C.; Bulović, V.; Grozema, F. C.; Stranks, S. D.; Hutter, E. M.; Savenije, T. J.; Osherov, A. Direct–Indirect Character of the Bandgap in Methylammonium Lead Iodide Perovskite. *Nat. Mater.* **2016**, *16* (1), 115–120. https://doi.org/10.1038/nmat4765.

(24) Sarritzu, V.; Sestu, N.; Marongiu, D.; Chang, X.; Wang, Q.; Masi, S.; Colella, S.; Rizzo, A.; Gocalinska, A.; Pelucchi, E.; et al. Direct or Indirect Bandgap in Hybrid Lead Halide Perovskites? *Adv. Opt. Mater.* **2018**, *6* (10), 1–8. https://doi.org/10.1002/adom.201701254.

(25) Green, M. A.; Ho-Baillie, A.; Snaith, H. J. The Emergence of Perovskite Solar Cells. *Nat. Photonics* **2014**, *8* (7), 506–514. https://doi.org/10.1038/nphoton.2014.134.

(26) Xing, G.; Mathews, N.; Sun, S.; Lim, S. S.; Lam, Y. M.; Grätzel, M.; Mhaisalkar, S.; Sum, T. C. Long-Range Balanced Electron- and Hole-Transport Lengths in Organic-Inorganic CH3NH3PbI3. *Science* **2013**, *342* (6156), 344–347. https://doi.org/10.1126/science.1243167.

(27) Saba, M.; Cadelano, M.; Marongiu, D.; Chen, F.; Sarritzu, V.; Sestu, N.; Figus, C.; Aresti, M.; Piras, R.; Geddo Lehmann, A.; et al. Correlated Electron-Hole Plasma in Organometal Perovskites. *Nat. Commun.* **2014**, *5* (May). https://doi.org/10.1038/ncomms6049.

(28) DeQuilettes, D. W.; Jariwala, S.; Burke, S.; Ziffer, M. E.; Wang, J. T. W.; Snaith, H. J.; Ginger, D. S. Tracking Photoexcited Carriers in Hybrid Perovskite Semiconductors: Trap-Dominated Spatial Heterogeneity and Diffusion. *ACS Nano* **2017**, *11* (11), 11488–11496. https://doi.org/10.1021/acsnano.7b06242.

(29) Li, B.; Ferguson, V.; Silva, S. R. P.; Zhang, W. Defect Engineering toward Highly Efficient and Stable Perovskite Solar Cells. *Adv. Mater. Interfaces* **2018**, *1800326*, 1800326. https://doi.org/10.1002/admi.201800326.

(30) Ball, J. M.; Petrozza, A. Defects in Perovskite-Halides and Their Effects in Solar Cells. *Nat. Energy* **2016**, *1* (11). https://doi.org/10.1038/nenergy.2016.149.

(31) Meggiolaro, D.; Motti, S.; Mosconi, E.; barker, A.; Ball, J.; Perini, C. A. R.; Deschler, F.; Petrozza, A.; De Angelis, F. Iodine Chemistry Determines the Defect Tolerance of Lead-Halide Perovskites. *Energy Environ. Sci.* **2018**, *11*, 702–713. https://doi.org/10.1039/C8EE00124C.

(32) Steirer, K. X.; Schulz, P.; Teeter, G.; Stevanovic, V.; Yang, M.; Zhu, K.; Berry, J. J. Defect Tolerance in Methylammonium Lead Triiodide Perovskite. *ACS Energy Lett.* **2016**, *1* (2), 360–366. https://doi.org/10.1021/acsenergylett.6b00196.

(33) Zhang, X.; Turiansky, M. E.; Van de Walle, C. G. Correctly Assessing Defect Tolerance in Halide Perovskites. *J. Phys. Chem. C* **2020**, *2020* (1). https://doi.org/10.1021/acs.jpcc.0c01324.

(34) Azpiroz, J. M.; Mosconi, E.; Bisquert, J.; De Angelis, F. Defect Migration in Methylammonium Lead Iodide and Its Role in Perovskite Solar Cell Operation. *Energy Environ. Sci.* **2015**, *8* (7), 2118–2127. https://doi.org/10.1039/c5ee01265a.

(35) Walsh, A.; Scanlon, D. O.; Chen, S.; Gong, X. G.; Wei, S. H. Self-Regulation Mechanism for Charged Point Defects in Hybrid Halide Perovskites. *Angew. Chemie - Int. Ed.* **2015**, *54* (6), 1791–1794. https://doi.org/10.1002/anie.201409740.

(36) Yuan, Y.; Chae, J.; Shao, Y.; Wang, Q.; Xiao, Z.; Centrone, A.; Huang, J. Photovoltaic Switching Mechanism in Lateral Structure Hybrid Perovskite Solar Cells. *Adv. Energy Mater.* **2015**, *5* (15), 1–7. https://doi.org/10.1002/aenm.201500615.

(37) Li, C.; Guerrero, A.; Zhong, Y.; Gräser, A.; Luna, C. A. M.; Köhler, J.; Bisquert, J.; Hildner, R.; Huettner, S. Real-Time Observation of Iodide Ion Migration in Methylammonium Lead Halide Perovskites. *Small* **2017**, *13* (42), 1–10. https://doi.org/10.1002/smll.201701711.

(38) Phung, N.; Al-ashouri, A.; Meloni, S.; Mattoni, A.; Albrecht, S.; Unger, E. L.; Merdasa, A.; Abate, A. The Role of Grain Boundaries on Ionic Defect Migration in Metal Halide Perovskites. **2020**, *1903735*. https://doi.org/10.1002/aenm.201903735.

(39) Nie, W.; Blancon, J.-C.; Neukirch, A. J.; Appavoo, K.; Tsai, H.; Chhowalla, M.; Alam, M. A.; Sfeir, M. Y.; Katan, C.; Even, J.; et al. Light-Activated Photocurrent Degradation and Self-Healing in Perovskite Solar Cells. *Nat. Commun.* **2016**, *7* (1), 1–9. https://doi.org/10.1038/ncomms11574.

(40) Yuan, H.; Debroye, E.; Janssen, K.; Naiki, H.; Steuwe, C.; Lu, G.; Moris, M.; Orgiu, E.; Uji-I, H.; De Schryver, F.; et al. Degradation of Methylammonium Lead Iodide Perovskite Structures through Light and Electron Beam Driven Ion Migration. *J. Phys. Chem. Lett.* **2016**, *7* (3), 561–566. https://doi.org/10.1021/acs.jpclett.5b02828.

(41) Scheblykin, I. G. Small Number of Defects per Nanostructure Leads to “ Digital ” Quenching of Photoluminescence : The Case of Metal Halide Perovskites. *Adv. Energy Mater.* **2020**, *2001724*, 1–7. https://doi.org/10.1002/aenm.202001724.

(42) Li, J.; Dobrovolsky, A.; Merdasa, A.; Unger, E. L.; Scheblykin, I. G. Luminescent Intermediates and Humidity-Dependent Room-Temperature Conversion of the MAPbI 3 Perovskite Precursor. *ACS Omega* **2018**, *3* (10), 14494–14502. https://doi.org/10.1021/acsomega.8b01799.

(43) Tavakoli, M. M.; Gu, L.; Gao, Y.; Reckmeier, C.; He, J.; Rogach, A. L.; Yao, Y.; Fan, Z. Fabrication of Efficient Planar Perovskite Solar Cells Using a One-Step Chemical Vapor Deposition Method. *Sci. Rep.* **2015**, *5* (May), 1–9. https://doi.org/10.1038/srep14083.

(44) Zhao, Y.; Nardes, A. M.; Zhu, K. Solid-State Mesostructured Perovskite CH3NH3PbI 3 Solar Cells: Charge Transport, Recombination, and Diffusion Length. *J. Phys. Chem. Lett.* **2014**, *5* (3), 490–494. https://doi.org/10.1021/jz500003v.

(45) Munir, R.; Sheikh, A. D.; Abdelsamie, M.; Hu, H.; Yu, L.; Zhao, K.; Kim, T.; Tall, O. El; Li, R.; Smilgies, D. M.; et al. Hybrid Perovskite Thin-Film Photovoltaics: In Situ Diagnostics and Importance of the Precursor Solvate Phases. *Adv. Mater.* **2017**, *29* (2). https://doi.org/10.1002/adma.201604113.

(46) Zhao, Y.; Zhu, K. CH3NH3Cl-Assisted One-Step Solution Growth of CH 3NH3PbI3: Structure, Charge-Carrier Dynamics, and Photovoltaic Properties of Perovskite Solar Cells. *J. Phys. Chem. C* **2014**, *118* (18), 9412–9418. https://doi.org/10.1021/jp502696w.

(47) Pellet, N.; Gao, P.; Gregori, G.; Yang, T. Y.; Nazeeruddin, M. K.; Maier, J.; Grätzel, M. Mixed-Organic-Cation Perovskite Photovoltaics for Enhanced Solar-Light Harvesting. *Angew. Chemie - Int. Ed.* **2014**, *53* (12), 3151–3157. https://doi.org/10.1002/anie.201309361.

(48) Stranks, S. D.; Eperon, G. E.; Grancini, G.; Menelaou, C.; Alcocer, M. J. P.; Leijtens, T.; Herz, L. M.; Petrozza, A.; Snaith, H. J. Electron-Hole Diffusion Lengths Exceeding 1 Micrometer in an Organometal Trihalide Perovskite Absorber. *Science (80-.).* **2013**, *342* (2013), 341–344. https://doi.org/10.1126/science.1243982.

(49) Feldmann, S.; Macpherson, S.; Senanayak, S. P.; Abdi-Jalebi, M.; Rivett, J. P. H.; Nan, G.; Tainter, G. D.; Doherty, T. A. S.; Frohna, K.; Ringe, E.; et al. Photodoping through Local Charge Carrier Accumulation in Alloyed Hybrid Perovskites for Highly Efficient Luminescence. *Nat. Photonics* **2019**. https://doi.org/10.1038/s41566-019-0546-8.

(50) Knight, A. J.; Patel, J. B.; Snaith, H. J.; Johnston, M. B.; Herz, L. M. Trap States, Electric Fields, and Phase Segregation in Mixed-Halide Perovskite Photovoltaic Devices. *Adv. Energy Mater.* **2020**, *10* (9), 1–11. https://doi.org/10.1002/aenm.201903488.

(51) Konstantakou, M.; Perganti, D.; Falaras, P.; Stergiopoulos, T. Anti-Solvent Crystallization Strategies for Highly Efficient Perovskite Solar Cells. *Crystals* **2017**, *7* (10), 291. https://doi.org/10.3390/cryst7100291.

(52) Jeon, N. J.; Noh, J. H.; Kim, Y. C.; Yang, W. S.; Ryu, S.; Seok, S. Il. Solvent Engineering for High-Performance Inorganic–Organic Hybrid Perovskite Solar Cells. *Nat. Mater.* **2014**, *13* (9), 897–903. https://doi.org/10.1038/nmat4014.

(53) Ren, Y.; Duan, B.; Xu, Y.; Huang, Y.; Li, Z.; Hu, L.; Hayat, T.; Wang, H.; Zhu, J.; Dai, S. New Insight into Solvent Engineering Technology from Evolution of Intermediates via One-Step Spin-Coating Approach. *Sci. China Mater.* **2017**, *60* (5), 392–398. https://doi.org/10.1007/s40843-017-9027-1.

(54) Yang, B.; Dyck, O.; Poplawsky, J.; Keum, J.; Das, S.; Puretzky, A.; Aytug, T.; Joshi, P. C.; Rouleau, C. M.; Duscher, G.; et al. Controllable Growth of Perovskite Films by Room-Temperature Air Exposure for Efficient Planar Heterojunction Photovoltaic Cells. *Angew. Chemie - Int. Ed.* **2015**, *54* (49), 14862–14865. https://doi.org/10.1002/anie.201505882.

(55) Liang, K.; Mitzi, D. B.; Prikas, M. T. Synthesis and Characterization of Organic-Inorganic Perovskite Thin Films Prepared Using a Versatile Two-Step Dipping Technique. *Chem. Mater.* **1998**, *10* (1), 403–411. https://doi.org/10.1021/cm970568f.

(56) Schlipf, J.; Docampo, P.; Schaffer, C. J.; Körstgens, V.; Bießmann, L.; Hanusch, F.; Giesbrecht, N.; Bernstorff, S.; Bein, T.; Müller-Buschbaum, P. A Closer Look into Two-Step Perovskite Conversion with X-Ray Scattering. *J. Phys. Chem. Lett.* **2015**, *6* (7), 1265–1269. https://doi.org/10.1021/acs.jpclett.5b00329.

(57) Ko, H.-S.; Lee, J.-W.; Park, N.-G.; Kim, H.-S.; Lee, C.-R.; Im, J.-H.; Lee, K.-B.; Moehl, T.; Marchioro, A.; Moon, S.-J.; et al. 15.76% Efficiency Perovskite Solar Cells Prepared under High Relative Humidity: Importance of PbI_2 Morphology in Two-Step Deposition of $CH_3NH_3PbI_3$. *J. Mater. Chem. A* **2015**, *3* (16), 8808–8815. https://doi.org/10.1039/C5TA00658A.

(58) Haruyama, J.; Sodeyama, K.; Han, L.; Tateyama, Y. Surface Properties of CH3NH3PbI3 for Perovskite Solar Cells. *Acc Chem Res* **2016**, *49* (3), 554–561. https://doi.org/10.1021/acs.accounts.5b00452.

(59) Leyden, M. R.; Jiang, Y.; Qi, Y. Chemical Vapor Deposition Grown Formamidinium Perovskite Solar Modules with High Steady State Power and Thermal Stability. *J. Mater. Chem. A* **2016**, *4* (34), 13125–13132. https://doi.org/10.1039/C6TA04267H.

(60) Jung, M.; Ji, S. G.; Kim, G.; Seok, S. Il. Perovskite Precursor Solution Chemistry: From Fundamentals to Photovoltaic Applications. *Chem. Soc. Rev.* **2019**, *48* (7), 2011–2038. https://doi.org/10.1039/c8cs00656c.

(61) Wang, B.; Wong, Y. K.; Yang, S.; Chen, T. Crystallinity and Defect State Engineering in Organo-Lead Halide Perovskite for High-Efficiency Solar Cells. *J. Mater. Chem. A* **2016**, *4* (10), 3806–3812. https://doi.org/10.1039/C5TA09249C.

(62) Yu, H.; Liu, X.; Xia, Y.; Dong, Q.; Zhang, K.; Wang, Z.; Zhou, Y.; Song, B.; Li, Y. Room-Temperature Mixed-Solvents-Vapor Annealing for High Performance Perovskite Solar Cells. *J. Mater. Chem. A* **2015**, *4*, 321–326. https://doi.org/10.1039/C5TA08565A.

(63) Xiao, Z.; Dong, Q.; Bi, C.; Shao, Y.; Yuan, Y.; Huang, J. Solvent Annealing of Perovskite-Induced Crystal Growth for Photovoltaic-Device Efficiency Enhancement. *Adv. Mater.* **2014**, *26* (37), 6503–6509. https://doi.org/10.1002/adma.201401685.

(64) Guo, Y.; Shoyama, K.; Sato, W.; Matsuo, Y.; Inoue, K.; Harano, K.; Liu, C.; Tanaka, H.; Nakamura, E. Chemical Pathways Connecting Lead(II) Iodide and Perovskite via Polymeric Plumbate(II) Fiber. *J. Am. Chem. Soc.* **2015**, *137* (50), 15907–15914. https://doi.org/10.1021/jacs.5b10599.

(65) Petrov, A. A.; Sokolova, I. P.; Belich, N. A.; Peters, G. S.; Dorovatovskii, P. V.; Zubavichus, Y. V.; Khrustalev, V. N.; Petrov, A. V.; Grätzel, M.; Goodilin, E. A.; et al. Crystal Structure of DMF-Intermediate Phases Uncovers the Link between CH3NH3PbI3Morphology and Precursor Stoichiometry. *J. Phys. Chem. C* **2017**, *121* (38), 20739–20743. https://doi.org/10.1021/acs.jpcc.7b08468.

(66) Park, S.-J.; Kim, A.-R.; Hong, J. T.; Park, J.-Y.; Lee, S.; Ahn, Y. H. Crystallization Kinetics of Lead Halide Perovskite Film Monitored by In-Situ Terahertz Spectroscopy. *J. Phys. Chem. Lett.* **2017**, acs.jpclett.6b02691. https://doi.org/10.1021/acs.jpclett.6b02691.

(67) Fateev, S. A.; Petrov, A. A.; Khrustalev, V. N.; Dorovatovskii, P. V.; Zubavichus, Y. V.; Goodilin, E. A.; Tarasov, A. B. Solution Processing of Methylammonium Lead Iodide Perovskite from γ-Butyrolactone: Crystallization Mediated by Solvation Equilibrium. *Chem. Mater.* **2018**, *30* (15), 5237–5244. https://doi.org/10.1021/acs.chemmater.8b01906.

(68) Even, J.; Pedesseau, L.; Katan, C. Analysis of Multivalley and Multibandgap Absorption and Enhancement of Free Carriers Related to Exciton Screening in Hybrid Perovskites. *J. Phys. Chem. C* **2014**, *118* (22), 11566–11572. https://doi.org/10.1021/jp503337a.

(69) You, J.; Hong, Z.; Yang, Y.; Chen, Q.; Cai, M.; Song, T.-B.; Chen, C.-C.; Lu, S.; Liu, Y.; Zhou, H.; et al. Low-Temperature Solution-Processed Perovskite Solar Cells with High Efficiency and Flexibility. *ACS Nano* **2014**, *8* (2), 1674–1680. https://doi.org/10.1021/nn406020d.

(70) Rehman, W.; McMeekin, D. P.; Patel, J. B.; Milot, R. L.; Johnston, M. B.; Snaith, H. J.; Herz, L. M. Photovoltaic Mixed-Cation Lead Mixed-Halide Perovskites: Links between Crystallinity, Photo-Stability and Electronic Properties. *Energy Environ. Sci.* **2017**, *10* (1), 361–369. https://doi.org/10.1039/c6ee03014a.

(71) Dong, W.; Hui-Min, Z.; Zhong-Min, Z.; Zai-Wei, W.; Si-Liu, L.; Shu-Ping, P.; Guang-Lei, C. Effect of Solvent on the Perovskite Thin Film Morphology and Crystallinity. *Acta Phys. Sin.* **2015**, *64* (24), 1–8. https://doi.org/10.7498/aps.64.038403.

(72) Zhou, Y.; Yang, M.; Wu, W.; Vasiliev, A. L.; Zhu, K.; Padture, N. P. Room-Temperature Crystallization of Hybrid-Perovskite Thin Films via Solvent-Solvent Extraction for High-Performance Solar Cells. *J. Mater. Chem. A* **2015**, *3*, 8178–8184. https://doi.org/10.1039/C5TA00477B.

(73) Eperon, G. E.; Habisreutinger, S. N.; Leijtens, T.; Bruijnaers, B. J.; Van Franeker, J. J.; Dequilettes, D. W.; Pathak, S.; Sutton, R. J.; Grancini, G.; Ginger, D. S.; et al. The Importance of Moisture in Hybrid Lead Halide Perovskite Thin Film Fabrication. *ACS Nano* **2015**, *9* (9), 9380–9393. https://doi.org/10.1021/acsnano.5b03626.

(74) Zhu, Z.; Hadjiev, V. G.; Rong, Y.; Guo, R.; Cao, B.; Tang, Z.; Qin, F.; Li, Y.; Wang, Y.; Hao, F.; et al. Interaction of Organic Cation with Water Molecule in Perovskite MAPbI3: From Dynamic Orientational Disorder to Hydrogen Bonding. *Chem. Mater.* **2016**, *28* (20), 7385–7393. https://doi.org/10.1021/acs.chemmater.6b02883.

(75) Li, D.; Bretschneider, S. A.; Bergmann, V. W.; Hermes, I. M.; Mars, J.; Klasen, A.; Lu, H.; Tremel, W.; Mezger, M.; Butt, H. J.; et al. Humidity-Induced Grain Boundaries in MAPbI3 Perovskite Films. *J. Phys. Chem. C* **2016**, *120* (12), 6363–6368. https://doi.org/10.1021/acs.jpcc.6b00335.

(76) Gangishetty, M. K.; Scott, R. W. J.; Kelly, T. L. Effect of Relative Humidity on Crystal Growth, Device Performance and Hysteresis in Planar Heterojunction Perovskite Solar Cells. *Nanoscale* **2016**, *8* (12), 6300–6307. https://doi.org/10.1039/C5NR04179A.

(77) Wang, B.; Zhang, Z.-G.; Ye, S.; Rao, H.; Bian, Z.; Huang, C.; Li, Y. Room-Temperature Water-Vapor Annealing for High-Performance Planar Perovskite Solar Cells. *J. Mater. Chem. A* **2016**, *4* (44), 17267–17273. https://doi.org/10.1039/C6TA08655A.

(78) Yuan, Y.; Wang, Q.; Shao, Y.; Lu, H.; Li, T.; Gruverman, A.; Huang, J. Electric-Field-Driven Reversible Conversion between Methylammonium Lead Triiodide Perovskites and Lead Iodide at Elevated Temperatures. *Adv. Energy Mater.* **2016**, *6* (2), 1–7. https://doi.org/10.1002/aenm.201501803.

(79) Besleaga, C.; Abramiuc, L. E.; Stancu, V.; Tomulescu, A. G.; Sima, M.; Trinca, L.; Plugaru, N.; Pintilie, L.; Nemnes, G. A.; Iliescu, M.; et al. Iodine Migration and Degradation of Perovskite Solar Cells Enhanced by Metallic Electrodes. *J. Phys. Chem. Lett.* **2016**, *7* (24), 5168–5175. https://doi.org/10.1021/acs.jpclett.6b02375.

(80) Bae, S.; Kim, S.; Lee, S. W.; Cho, K. J.; Park, S.; Lee, S.; Kang, Y.; Lee, H. S.; Kim, D. Electric-Field-Induced Degradation of Methylammonium Lead Iodide Perovskite Solar Cells. *J. Phys. Chem. Lett.* **2016**, *7* (16), 3091–3096. https://doi.org/10.1021/acs.jpclett.6b01176.

(81) Zhao, J.; Deng, Y.; Wei, H.; Zheng, X.; Yu, Z.; Shao, Y.; Shield, J. E.; Huang, J. Strained Hybrid Perovskite Thin Films and Their Impact on the Intrinsic Stability of Perovskite Solar Cells. *Sci. Adv.* **2017**, *3* (11). https://doi.org/10.1126/sciadv.aao5616.

(82) Jones, T. W.; Osherov, A.; Alsari, M.; Sponseller, M.; Duck, B. C.; Jung, Y. K.; Settens, C.; Niroui, F.; Brenes, R.; Stan, C. V.; et al. Lattice Strain Causes Non-Radiative Losses in Halide Perovskites. *Energy Environ. Sci.* **2019**, *12* (2), 596–606. https://doi.org/10.1039/c8ee02751j.

(83) Li, X.; Luo, Y.; Holt, M. V.; Cai, Z.; Fenning, D. P. Residual Nanoscale Strain in Cesium Lead Bromide Perovskite Reduces Stability and Shifts Local Luminescence. *Chem. Mater.* **2019**, *31* (8), 2778–2785. https://doi.org/10.1021/acs.chemmater.8b04937.

(84) Zhu, C.; Niu, X.; Fu, Y.; Li, N.; Hu, C.; Chen, Y.; He, X.; Na, G.; Liu, P.; Zai, H.; et al. Strain Engineering in Perovskite Solar Cells and Its Impacts on Carrier Dynamics. *Nat. Commun.* **2019**, *10* (1). https://doi.org/10.1038/s41467-019-08507-4.

(85) Zhao, J.; Liu, M.; Fang, L.; Jiang, S.; Zhou, J.; Ding, H.; Huang, H.; Wen, W.; Luo, Z.; Zhang, Q.; et al. Great Disparity in Photoluminesence Quantum Yields of Colloidal CsPbBr 3 Nanocrystals with Varied Shape: The Effect of Crystal Lattice Strain. *J. Phys. Chem. Lett.* **2017**, *8* (13), 3115–3121. https://doi.org/10.1021/acs.jpclett.7b01083.

(86) Rolston, N.; Bush, K. A.; Printz, A. D.; Gold-Parker, A.; Ding, Y.; Toney, M. F.; McGehee, M. D.; Dauskardt, R. H. Engineering Stress in Perovskite Solar Cells to Improve Stability. *Adv. Energy Mater.* **2018**, *8* (29), 1–7. https://doi.org/10.1002/aenm.201802139.

(87) Wu, C.; Chen, K.; Guo, D. Y.; Wang, S. L.; Li, P. G. Cations Substitution Tuning Phase Stability in Hybrid Perovskite Single Crystals by Strain Relaxation. *RSC Adv.* **2018**, *8* (6), 2900–2905. https://doi.org/10.1039/c7ra12521f.

(88) Capitani, F.; Marini, C.; Caramazza, S.; Postorino, P.; Garbarino, G.; Hanfland, M.; Pisanu, A.; Quadrelli, P.; Malavasi, L. High-Pressure Behavior of Methylammonium Lead Iodide (MAPbI3) Hybrid Perovskite. *J. Appl. Phys.* **2016**, *119* (18). https://doi.org/10.1063/1.4948577.

(89) Zhang, L.; Zeng, Q.; Wang, K. Pressure-Induced Structural and Optical Properties of Inorganic Halide Perovskite CsPbBr 3. *J. Phys. Chem. Lett.* **2017**, *8* (16), 3752–3758. https://doi.org/10.1021/acs.jpclett.7b01577.

(90) Grote, C.; Berger, R. F. Strain Tuning of Tin-Halide and Lead-Halide Perovskites: A First-Principles Atomic and Electronic Structure Study. *J. Phys. Chem. C* **2015**, *119* (40), 22832–22837. https://doi.org/10.1021/acs.jpcc.5b07446.

(91) Zhang, L.; Geng, W.; Tong, C. J.; Chen, X.; Cao, T.; Chen, M. Strain Induced Electronic Structure Variation in Methyl-Ammonium Lead Iodide Perovskite. *Sci. Rep.* **2018**, *8* (1), 1–9. https://doi.org/10.1038/s41598-018-25772-3.

(92) Yuan, X.; Jing, P.; Li, J.; Wei, M.; Hua, J.; Zhao, J.; Tian, L.; Li, J. Temperature-Dependent Photoluminescence of Inorganic Perovskite Nanocrystal Films. *RSC Adv.* **2016**, *6* (82), 78311–78316. https://doi.org/10.1039/c6ra17008k.

(93) Zheng, H.; Dai, J.; Duan, J.; Chen, F.; Zhu, G.; Wang, F.; Xu, C. Temperature-Dependent Photoluminescence Properties of Mixed-Cation Methylammonium-Formamidium Lead Iodide [HC(NH2)2]:X[CH3NH3]1-XPbI3 Perovskite Nanostructures. *J. Mater. Chem. C* **2017**, *5* (46), 12057–12061. https://doi.org/10.1039/c7tc04146b.

(94) Woo, H. C.; Choi, J. W.; Shin, J.; Chin, S. H.; Ann, M. H.; Lee, C. L. Temperature-Dependent Photoluminescence of CH3NH3PbBr3 Perovskite Quantum Dots and Bulk Counterparts. *J. Phys. Chem. Lett.* **2018**, *9* (14), 4066–4074. https://doi.org/10.1021/acs.jpclett.8b01593.

(95) Gerhard, M.; Louis, B.; Camacho, R.; Merdasa, A.; Li, J.; Kiligaridis, A.; Dobrovolsky, A.; Hofkens, J.; Scheblykin, I. G. Microscopic Insight into Non-Radiative Decay in Perovskite Semiconductors from Temperature-Dependent Luminescence Blinking. *Nat. Commun.* **2019**, *10* (1), 1698. https://doi.org/10.1038/s41467-019-09640-w.

(96) Osherov, A.; Hutter, E. M.; Galkowski, K.; Brenes, R.; Maude, D. K.; Nicholas, R. J.; Plochocka, P.; Bulović, V.; Savenije, T. J.; Stranks, S. D. The Impact of Phase Retention on the Structural and Optoelectronic Properties of Metal Halide Perovskites. *Adv. Mater.* **2016**, *28* (48), 10757–10763. https://doi.org/10.1002/adma.201604019.

(97) Samanta, A. Dynamic Stokes Shift and Excitation Wavelength Dependent Fluorescence of Dipolar Molecules in Room Temperature Ionic Liquids. *J. Phys. Chem. B* **2006**, *110* (28), 13704–13716. https://doi.org/10.1021/jp060441q.

(98) Tian, Y.; Merdasa, A.; Peter, M.; Abdellah, M.; Zheng, K.; Ponseca Jr., C. S.; Pullerits, T.; Yartsev, A.; Sundstrom, V.; Scheblykin, I. G. Giant Photoluminescence Blinking of Perovskite Nanocrystals Reveals Single-Trap Control of Luminescence. *Nano Lett* **2015**, *15* (3), 1603–1608. https://doi.org/10.1021/nl5041397.

(99) Dobrovolsky, A.; Merdasa, A.; Unger, E. L.; Yartsev, A.; Scheblykin, I. G. Defect-Induced Local Variation of Crystal Phase Transition Temperature in Metal-Halide Perovskites. *Nat. Commun.* **2017**, *8* (1), 34. https://doi.org/10.1038/s41467-017-00058-w.

(100) Manser, J. S.; Saidaminov, M. I.; Christians, J. A.; Bakr, O. M.; Kamat, P. V. Making and Breaking of Lead Halide Perovskites. *Acc Chem Res* **2016**, *49* (2), 330–338. https://doi.org/10.1021/acs.accounts.5b00455.

(101) Shoyama, K.; Sato, W.; Guo, Y.; Nakamura, E. Effects of Water on the Forward and Backward Conversions of Lead(<scp>ii</Scp>) Iodide to Methylammonium Lead Perovskite. *J. Mater. Chem. A* **2017**, *5* (c), 23815–23821. https://doi.org/10.1039/C7TA08042E.

(102) Dubey, A.; Kantack, N.; Adhikari, N.; Reza, K. M.; Venkatesan, S.; Kumar, M.; Khatiwada, D.; Darling, S.; Qiao, Q. Room Temperature, Air Crystallized Perovskite Film for High Performance Solar Cells. *J. Mater. Chem. A* **2016**, *4* (26), 10231–10240. https://doi.org/10.1039/C6TA02918C.

(103) Merdasa, A.; Tian, Y.; Camacho, R.; Dobrovolsky, A.; Debroye, E.; Unger, E. L.; Hofkens, J.; Sundström, V.; Scheblykin, I. G. "supertrap" at Work: Extremely Efficient Nonradiative Recombination Channels in MAPbI3Perovskites Revealed by Luminescence Super-Resolution Imaging and Spectroscopy. *ACS Nano* **2017**, *11* (6), 5391–5404. https://doi.org/10.1021/acsnano.6b07407.

(104) Eremchev, I. Y.; Tarasevich, A. O.; Li, J.; Naumov, A. V; Scheblykin, I. G. Lack of Photon Antibunching Supports Supertrap Model of Photoluminescence Blinking in Perovskite Sub-Micrometer Crystals. *Adv. Opt. Mater.* **2020**, *2001596* (2001596). https://doi.org/10.1002/adom.202001596.